

Dudley Knox Library, NPS
Monterey, CA 93943

NAVAL POSTGRADUATE SCHOOL

Monterey, California



THESIS

AN INVESTIGATION OF CASCADE ENERGY DENSITY
EFFECTS USING CLASSICAL TRAJECTORY
SIMULATIONS OF SPUTTERING
BY MOLECULAR IONS

by

William A. Mason

June 1983

Thesis Advisor: Don E. Harrison, Jr.

Approved for public release; distribution unlimited

T208840

REPORT DOCUMENTATION PAGE		READ INSTRUCTIONS BEFORE COMPLETING FORM
1. REPORT NUMBER	2. GOVT ACCESSION NO.	3. RECIPIENT'S CATALOG NUMBER
4. TITLE (and Subtitle) An Investigation of Cascade Energy Density Effects Using Classical Trajectory Simulations of Sputtering by Molecular Ions		5. TYPE OF REPORT & PERIOD COVERED Masters Thesis June 1983
7. AUTHOR(s) William A. Mason		6. PERFORMING ORG. REPORT NUMBER
9. PERFORMING ORGANIZATION NAME AND ADDRESS Naval Postgraduate School Monterey, CA. 93940		8. CONTRACT OR GRANT NUMBER(s)
11. CONTROLLING OFFICE NAME AND ADDRESS Naval Postgraduate School Monterey, CA. 93940		10. PROGRAM ELEMENT, PROJECT, TASK AREA & WORK UNIT NUMBERS
14. MONITORING AGENCY NAME & ADDRESS (if different from Controlling Office)		12. REPORT DATE June 1983
		13. NUMBER OF PAGES 91
		15. SECURITY CLASS. (of this report) UNCLASSIFIED
		15a. DECLASSIFICATION/DOWNGRADING SCHEDULE
16. DISTRIBUTION STATEMENT (of this Report) Approved for public release; distribution unlimited		
17. DISTRIBUTION STATEMENT (of the abstract entered in Block 20, if different from Report)		
18. SUPPLEMENTARY NOTES		
19. KEY WORDS (Continue on reverse side if necessary and identify by block number) Sputtering Computer Simulation Molecular Ion		
20. ABSTRACT (Continue on reverse side if necessary and identify by block number) The NPS computer simulation model was modified to study sputtering by molecular ions. The simulations were performed on a Cu(111) surface for normally incident O ₂ ions at 0.5, 1.25, 2.5, and 5.0 kev/ion. The molecule's angular orientation was both set at specific values and randomly determined. The normalized energy distributions of sputtered atoms for two energy ranges, 0-20 and 0-3 ev/sputtered atom, and the		

Block 20 (cont'd)

sputtering yield ratios were investigated. The 0-20 ev/sputtered atom energy distributions show distinct peaks at 1.8 ev which are insensitive to incident energy, energy density, and molecular orientation. Simulations indicate that there may be fine structure in the 0-3 ev/sputtered atom range with a cascade interaction unique to molecular sputtering. For a number of molecular orientations which produce very different cascade overlaps, the sputtering yield ratios do not correlate with the degree of overlap. The energy density of a cascade is not an accurate predictor of the sputtering yield ratio.

Approved for public release; distribution unlimited

An Investigation of Cascade Energy Density Effects
Using Classical Trajectory Simulations of
Sputtering by Molecular Ions

by

William A. Mason
Lieutenant, United States Navy
B.S., University of Utah, 1977

Submitted in partial fulfillment of the
requirements for the degree of

MASTER OF SCIENCE IN PHYSICS

from the

NAVAL POSTGRADUATE SCHOOL
June 1983

ABSTRACT

The NPS computer simulation model was modified to study sputtering by molecular ions. The simulations were performed on a Cu(111) surface for normally incident O_2^+ ions at 0.5, 1.25, 2.5, and 5.0 kev/ion. The molecule's angular orientation was both set at specific values and randomly determined. The normalized energy distributions of sputtered atoms for two energy ranges, 0-20 and 0-3 ev/sputtered atom, and the sputtering yield ratios were investigated. The 0-20 ev/sputtered atom energy distributions show distinct peaks at 1.8 ev which are insensitive to incident energy, energy density, and molecular orientation. Simulations indicate that there may be fine structure in the 0-3 ev/sputtered atom range with a cascade interaction unique to molecular sputtering. For a number of molecular orientations which produce very different cascade overlaps, the sputtering yield ratios do not correlate with the degree of overlap. The energy density of a cascade is not an accurate predictor of the sputtering yield ratio.

TABLE OF CONTENTS

I.	INTRODUCTION -----	7
II.	OBJECTIVES -----	16
III.	THE MODEL -----	18
	A. BACKGROUND -----	18
	B. INPUT PARAMETERS -----	20
	C. MICROCRYSTAL -----	22
	D. ORIENTATION OF THE MOLECULE -----	23
	E. IMPACT AREA -----	25
	F. ENERGIES -----	26
	G. POTENTIAL FUNCTIONS -----	27
IV.	DISCUSSION AND RESULTS -----	29
	A. ENERGY DISTRIBUTIONS -----	29
	B. ANGULAR DISTRIBUTIONS -----	34
	C. SPUTTERING YIELD RATIOS -----	36
	D. EFFECTS OF MOLECULAR ORIENTATION -----	37
	E. OTHER MOLECULAR EFFECTS -----	40
	F. THE MODEL -----	42
V.	CONCLUSIONS -----	43
	A. THE MODEL -----	43
	B. SPUTTERED ATOM NORMALIZED ENERGY DISTRIBUTIONS -----	43
	C. YIELD RATIOS -----	44
	D. MOLECULAR ORIENTATION -----	45

VI.	RECOMMENDATIONS -----	46
A.	THE MODEL -----	46
B.	SPUTTERED ATOM NORMALIZED ENERGY DISTRIBUTIONS -----	46
C.	YIELD RATIOS -----	47
D.	ION-ATOM POTENTIAL FUNCTION -----	48
	REFERENCES -----	49
	FIGURES -----	52
	INITIAL DISTRIBUTION LIST -----	91

I. INTRODUCTION

A. OVERVIEW

Sputtering, the ejection of atoms from a solid by energetic ion bombardment, is caused by the collision of incident ions with atoms in the surface and near-surface layers.

Sputtering was first observed by Grove [1] in 1852. While conducting experiments with electrical discharges in a low-pressure gas, he noticed that cathode material was deposited on the inner wall of the discharge tube. Thus, sputtering gained its reputation as a contaminating side-effect of electrical discharge processes. This reputation persisted for nearly 100 years and scientific interest in the sputtering phenomenon was largely directed toward its elimination rather than its understanding. However, major scientific achievements in the 20th century, such as high voltage, high power radar transmitter tubes, focused attention on sputtering. Thereafter, sputtering research followed two parallel courses: First, the development of a basic theoretical understanding of the physics of sputtering, and the acquisition of experimental data. Second, exploitation of this knowledge for practical purposes.

Sputtering as a bulk, macroscopic process was "understood" and early applied to a limited degree. For example, the development of pumps based on ion trapping processes and the production of atomically clean surfaces. However, very little true understanding of the physics of sputtering was achieved through early experimentation or theoretical models.

B. EARLY EXPERIMENTATION

Experimental results proliferated but, in general, the data were plagued by non-reproducibility caused by inconsistent experimental conditions [2,3]. Penning and Moubis [4] first demonstrated conclusively the effect of ambient pressure on sputtering experiments. They also coupled a magnetic field to their discharge apparatus to reduce back-diffusion of sputtered material to the surface [4]. Their experiments produced the first consistently reproducible results for energies greater than 500 ev.

Surface cleanliness, the elimination of oxide layers or adsorbed gases, is a critical factor in sputtering experiments. Arifov, et. al., [5] demonstrated in controlled experiments the dependence of the sputtering yield on surface contamination. Yonts and Harrison [6] presented evidence indicating that surface recontamination from background gases is a significant factor in

quantitative sputtering yield measurements and developed criteria for "clean" surface experiments.

C. DEVELOPMENT OF ANALYTIC THEORY

Stark [7,8] first extensively discussed the concept of an individual sputtering event on an atomic scale and developed two competing models: He originated the hot-spot model which proposed the ejection of surface material from a microscopically small region due to evaporation at high local temperatures generated by ion impact [7]. His second, the collision model, described the sputtering event as a series of binary collisions initiated by a single incident ion. He applied the conservation laws for elastic collisions to this model and qualitatively described the energy dependence of the yield curve [8]. Stark obtained limited agreement with experiments at energies less than 1 kev.

Kingdon and Langmuir [9] further developed the binary collision momentum and energy model to describe the observed desorption of a thorium monolayer from a tungsten surface by ion bombardment.

In 1926, von Hippel [10] formally presented the hot-spot theory of sputtering which was further developed by Townes [11] in 1944. Townes' theory correlated well with some contemporary experimental results, but the agreement was subsequently shown to be fortuitous.

Keywell [12] developed a theory based upon the moderation of neutrons, which may be taken as a precursor of the collision cascade concept to follow. Harrison [13] developed the first direct statistical theory of sputtering which bridged the gap between the Kingdon and Langmuir momentum transfer theory and Townes' hot-spot theory. A significant feature of the Keywell and Harrison theories is the application of probability concepts as expressed by collision cross-sections.

At this point in the evolution of sputtering research, the vast majority of experimental data were based upon sputtering from polycrystalline surfaces [3]. Sputtering was assumed to be isotropic with the angular distribution of sputtered material following a cosine distribution. Effects due to the underlying crystal structure were not considered.

A major turning point in sputtering theory was the experimental demonstration of lattice effects in monocrystal sputtering. Wehner [14] showed that sputtering from single crystals proceeded in preferred directions which correlated with the directions of closest packing in the particular crystal. This sputtering anisotropy completely contradicted the hot-spot model and pointed to momentum transfer as the key ejection mechanism. Silsbee's focusing collision model [15] quickly followed as a partial explanation for preferential ejection. In addition,

experimental results showed the sputtering yield to be strongly sensitive to the crystallographic direction of the incident ion beam. The subsequent discovery of channeling [16-20], and the elucidation of assisted focusing and replacement collision (previously known as crowdion) models [21] showed that even a single momentum transfer theory must be an aggregate of many different mechanisms.

D. COLLISION CASCADE THEORY

Sigmund [22,23] developed an extension of the statistical theory which displaced the focusing models. It is based upon a linearized form of the general Boltzmann transport equation. Sigmund's model treats an amorphous solid with a surface binding energy potential barrier. An incident ion strikes a surface atom and creates a collision cascade via binary collisions. An atom in the cascade sputters if it is headed outward from the surface and overcomes the surface potential barrier. In doing so, the atom's velocity vector is refracted away from the surface normal by the attractive surface binding energy. Significant agreement with high energy experimental results, that is, incident ion energy much greater than the surface binding energy, has been achieved. However, it has since been shown that the major result of the Sigmund theory follows immediately from a dimensional analysis of the system!

Thompson [24] and Robinson [25] have taken similar approaches while accounting for focusons and channeling, respectively, and have obtained comparable results.

The primary utility of the Sigmund and Thompson theories has been to provide experimentalists with simple formulae to apply to a wide variety of sputtering experiments. However, these theories fail to adequately predict sputtering yields at low energies [22,23,26]. The high-energy, binary collision model for the collision cascade does not account for the predominance of low-energy sputtered atoms from near-surface layers.

In general, the collision cascade can only be reasonably understood as a many-body, or multiple interaction (MI), process. However, the MI model cannot be solved analytically.

E. COMPUTER SIMULATION MODELS

Gibson, Goland, Milgram and Vineyard (GGMV) [27] first demonstrated the power and feasibility of the use of computer simulation techniques to model radiation damage experiments. Their computer program builds a finite, three-dimensional monocrystal lattice of copper, accelerates a lattice atom in a specific direction with specific energy, and solves the resultant MI cascade by applying numerical methods to Newton's equations of motion.

In this particular case, GGMV studied the generation of lattice vacancies and interstitials.

Robinson and Oen [16, 17] applied GGMV's prototype to ion range studies and demonstrated ion channeling, which was subsequently verified experimentally [18, 20].

Harrison expanded upon GGMV's concept and designed a simulation model to specifically study sputtering [28-32] with the flexibility to simulate a wide variety of experimental conditions. Harrison's early results showed that neither Focusons nor Sigmund's or Thompson's models accounted for the majority of sputtered atoms (see also the work of Lehmann and Sigmund [33]). Simulations show that the vast majority of sputtered atoms originate in the surface layer, and the results agree reasonably well with experimental yield data. Simulations augment laboratory results and allow the isolation and manipulation of variables not readily accessible in the lab [34, 35].

F. INTERATOMIC POTENTIAL FUNCTIONS

A primary thread of uncertainty that runs through each sputtering model and theory is the form of the interatomic potential function [3, 35, 36]. No single interatomic potential has yet been deduced which fits every sputtering experiment. Simulations are particularly well-suited for isolating, modifying, and observing the

sensitivity of the sputtering event to the nature of the interatomic potential [35, 37, 38].

G. NON-LINEAR CASCADE EFFECTS

Recent experimental results indicated that the analytic sputtering theories do not adequately predict the sputtering yield for heavy ions bombarding heavy targets [39-41]. A spike theory has emerged which states that linear cascade theory breaks down (becomes non-linear) when the average energy per atom in the cascade approaches the surface binding energy of the target material [42]. The spike model emphasizes random ejection effects from the region of high energy density. Kelly [43] proposes a thermal sputtering theory, a Renaissance of the hot-spot theory, to explain the non-linear effects in the context of the spike.

These theories reinforce the multiplicity of sputtering phenomena, but continue to fall short of providing a comprehensive analytic model.

H. MOLECULAR SPUTTERING

Bombardment by molecular ions is well-suited for investigating non-linear effects since the yield from a single ion can be compared to the yield from a molecular ion of the same element with the same energy per ion. Few published results of molecular sputtering exist [39-41, 44].

The available results do demonstrate non-linear effects but do not confirm the abnormally high yield enhancement addressed by the spike model [42].

It is not yet clear whether the individual ion cascades resulting from the molecule's dissociation upon impact overlap to significantly increase cascade energy density, or whether molecular orientation affects the sputtering mechanisms.

II. OBJECTIVES

Few results exist for molecular sputtering. Bader, et. al, [44] conducted low-energy (< 8 kev) experiments with N^+ and N_2^+ on several metals. Their primary objectives were to study the effects of the upper atmosphere on satellites and other space vehicles and to investigate erosion rates within ion propulsion drive systems. Recent experiments in non-linear cascade effects use high-energy (100-200 kev/ion) polyatomic molecules as a convenient method of increasing primary energy density in near-surface layers of polycrystalline targets [39-42]. No other experiments have been conducted to study the effects of molecular sputtering, per se.

The primary objective of this thesis is to study the sputtering of a copper monocrystal by low-energy (0.5 - 5.0 kev/ion) diatomic molecules using a computer simulation model.

More specifically, the following areas will be studied:

1. Comparison of energy and angular distributions of sputtered atoms, and absolute yields for molecular (O_2^+) and ion (O^+) bombardment.

2. Effects of molecular orientation upon the sputtering yield.

3. Comparison of $O_2^+/2O^+$ yield ratios with published results for $N_2^+/2N^+$ [44].

4. Comparison of $O_2^+/2O^+$ and $Ar_2^+/2Ar^+$ yield ratios for indication of yield enhancement in accordance with non-linear cascade theory [39-42].

5. Effects of mass ratio (M_1/M_2) and ion size (ion-atom potential) upon yield ratios.

6. Differences in incident ion scattering for molecular and ion bombardment.

7. Cascade overlap.

III. THE MODEL

A. BACKGROUND

QRAD, a full-lattice simulation computer program, is designed to model the dissipation of an incident ion's momentum, using classical mechanics, in a solid monocrystal [28-32]. See references [34] and [35] for detailed discussions of the theory and principles of simulation physics as applied to sputtering. This thesis is based upon the program QMOL, a slightly modified version of QRAD, which allows bombardment by diatomic, homonuclear molecules. The remainder of this section will be presented in terms of QRAD. The unique differences of QMOL will be discussed in following sections.

A note on terminology is instructive. Ion refers to a single atom incident upon the target. Molecule refers to a diatomic, homonuclear species of the same element as the ion incident upon the target. The molecule always dissociates upon impact. Immediately following impact, each fragment of the molecule is an ion. Atom refers to an atom of the monocrystal. A sput is a sputtered atom.

QRAD simulates a wide variety of experimental conditions. Each of the common metallic unit cells can be built and duplicated to form a monocrystal of up to 2500

atoms with a specific crystal plane exposed to the incident ion. Additionally, QRAD can model alloys, stepped surfaces, and adsorbed surface layers.

The ion, of given mass, is shot at the surface by assigning to it velocity components consistent with its angle of incidence and energy, and positioning it immediately above a specific impact point. Hamilton's equations of motion are solved numerically by an average force method [45] for the resultant MI collision cascade, or trajectory.

The trajectory advances by timesteps. During each timestep, the positions and velocities of the ion and atoms develop simultaneously. Each ion and atom is "looked at" and its motion and forces analyzed at the end of each time step. The "look" each receives depends upon its total energy and the total energy of its nearest neighbors. A hierarchy of three mini-logics corresponding to the depth of the "look" significantly reduces computer time compared with earlier generations of QRAD. The program flags all ions and atoms which rise above the surface. The trajectory terminates when the energy of the most energetic atom decreases to a specified value below which the probability of additional atoms rising above the surface is very small.

Each flagged ion or atom is tested by the program to determine whether it has sufficient outward momentum to

completely escape the surface into the "vacuum". Atoms and ions which pass this test are listed as sputtered and scattered, respectively. The program records the final positions and velocities of the sputs and scattered ions and restores the system so that another trajectory can be executed. Individual trajectories may be studied in detail to follow the sputtering process or identify the occurrence of other phenomena such as channeling.

Global results which may be compared to experimental data are obtained by averaging the results over N trajectories, where N is typically 80-100. The sample of trajectories is based upon N impact points uniformly distributed within an impact area chosen such that it is a representative symmetry area of the surface. The N trajectories determine sput yields, energy and angular distributions and the spatial distribution of yield over the impact area. Multimer formation is determined from additional sput analysis. Dimers and trimers are identified and listed with their energy and angular distributions.

B. INPUT PARAMETERS

Molecular data input parameters are listed and defined below so that their meanings will be clear in following sections.

1. Bullet parameter card

ion (1), ion (2)

chemical symbols of
constituent atoms

LSS = 0/3

flag:

0 = single incident ion

3 = incident molecule

THEM

θ_m , polar angle of
ion (2) with respect to
ion (1)

PHIM

ϕ_m , azimuthal angle of
ion (2) with respect to
ion (1)

SEP

ρ , interatomic separation
in angstroms.

IRANF = 0/1

flag for random molecule

ISEED

seed value for random
no. generator

2. Reconstruction card

IRECON = 0/1

flag for reconstruction
of trajectory

ITRJ

no. of trajectory to be
reconstructed

C. MICROCRYSTAL

A 360-atom copper (FCC) monocrystal is used for each simulation. The crystal is "cut" to expose the (111) plane to the incident molecule (Fig. 1). The crystal contains 4 layers with 90 atoms per layer and is designated (15x4x12): 15 planes wide, 4 planes thick, and 12 planes long. RYBL is the minimum positive distance an atom must rise above a surface before it is considered ejected. Note that the first numbered atom in the crystal is labelled atom 3 (Fig. 2). Atoms 1 and 2 comprise the molecule. When comparing QMOL and QRAD trajectories, $ATOM(x)_{QMOL} = ATOM(x-1)_{QRAD}$.

Containment, the ability of the target lattice to contain the entire collision cascade, is discussed elsewhere in detail [34]. The size of this microcrystal is a trade-off between asymptotic containment and reasonable computer run-time. A series of tests have determined that absolute yield containment requires approximately 150 atoms per layer at 1.0 kev and about 250 atoms per layer at 5.0 kev. Absolute containment of an event is paramount for an analytic description of the sputtering yield. However, it is less significant when studying mechanisms or observables such as yield ratios, and energy and angular distributions. Experience shows [28,-32, 34] that this lattice provides adequate containment for these observables at 0.50 to 5.0 kev per ion.

D. ORIENTATION OF THE MOLECULE

Figure 3 shows the orientation of the molecule with respect to the crystal axes. Note that the $-y$ axis is the outward normal for the (111) plane.

The molecule has 5 degrees of freedom. Angles θ_i and ϕ_i define the incident direction of the molecule. θ_m and ϕ_m , the polar and azimuthal angles respectively, and the interatomic separation, ρ , define the position of ion(2) relative to ion(1). Ion(2) is assigned the same velocity components as ion(1). Vibrational and rotational degrees of freedom are not included.

The ranges of the angles are $0 \leq \theta_m, \theta_i \leq \pi/2$ and $0 \leq \phi_m, \phi_i \leq 2\pi$. Therefore, ion(2) is always trailing ion (1) prior to impact. The molecule can assume any orientation with respect to the surface because ion(1) and ion(2) are identical. This procedure would not be suitable for an AB-type molecule such as CO. Each simulation was executed with the molecule normally incident upon the surface. θ_m and ϕ_m were set at specific values for some runs, but at random values for others to be more similar to experimental conditions. Some effects of beam polarization can be inferred from trajectories in which θ_m and ϕ_m are set at specific values : (1) transversely polarized molecule, $\theta_m = \pi/2, 0 \leq \phi_m \leq 2\pi$, (2) longitudinally polarized molecule, $\theta_m = \phi_m = 0$.

Random values of θ_m and ϕ_m are generated as follows:
 When IRANF is set, the program calls the library random number generator LRND which uses the value of ISEED to generate 5 random numbers. Four are used to calculate θ_m and ϕ_m by von Neumann's method:

$$\theta_m = \sin^{-1} \frac{2 R_1 R_2}{(R_1^2 + R_2^2)}$$

$$\phi_m = \sin^{-1} \frac{2 R_3 R_4}{(R_3^2 + R_4^2)}$$

where $0 \leq \theta_m, \phi_m \leq \pi/2$. The fifth sets $0 \leq \phi_m \leq \pi$ or $\pi < \phi_m \leq 2\pi$. LRND is called for each subsequent trajectory and uses its internally updated value of ISEED to generate the next set of random numbers.

The initial position of ion(2) with respect to the impact point is calculated as follows:

$$DPX = \rho \sin \theta_m \cos \phi_m$$

$$DPY = -\rho \cos \theta_m$$

$$DPZ = \rho \sin \theta_m \sin \phi_m.$$

The exact impact point of ion(2) is unknown prior to impact unless the molecule is transversely polarized. In all cases, ion(2)'s motion is perturbed by interaction with ion(1) at impact. Ion(2)'s impact point can be determined by examining the first 5-10 timesteps in the printed output of a trajectory reconstruction.

A random molecule trajectory is not reproducible unless the exact values of θ_m , ϕ_m , and ISEED are repeated from the

original trajectory. A specific trajectory is reconstructed as follows: When IRECON is set, the program calls LRND and executes a LRND loop ITRJ-times, where ITRJ is the number of the trajectory to be reconstructed. The program now holds the same set of 5 random numbers for trajectory ITRJ as in the original run and calculates θ_m and ϕ_m as before.

E. IMPACT AREA

The impact area for each simulation is a rectangle containing a grid of 104 uniformly distributed impact points (Fig. 4) and is a representative symmetry area of the entire (111) surface (Fig. 2). The impact area was designed for bombarding a stepped Ni (111) surface [46] and was adapted to this research to provide an extensive sampling area.

Note that the reference target point is centered on atom 36 (for QMOL) and is designated (RBX, RBZ) = (6, 4) in units of planes as measured from the origin at the center of atom 3. Likewise, the impact points, (SPX, SPZ), are in units of planes and are labelled in figure 4 with their corresponding trajectory numbers. Figure 5, drawn to scale, shows the complete grid of impact points superimposed on the surface with atom 44 centered in the

area. Note the positions of the atoms in the second layer.

Independent data sets can be generated from the 104-point data set by simple displacements from the original RBX/RBZ. Figures 6 and 7 show two sets of RBX/RBZ displacements which can generate 1-12 displaced data sets. The utility of the displaced data sets is to significantly increase the sput population for a particular simulation without significantly changing the position of the impact area. The increased populations reduce statistical fluctuations in energy and angular distributions.

F. ENERGIES

Recall that Bader, et. al., [44] conducted low-energy (< 8 kev/ion) molecular sputtering experiments, and that investigations of non-linear cascade effects have utilized high-energy (100-200 kev/ion) molecules. The simulations presented in this thesis were conducted at 0.50, 1.25, 2.50, and 5.00 kev/ion.

This is the first investigation of molecular sputtering using the latest-generation simulation model. An extensive data base of single-ion simulation sputtering experiments exists in this energy range. A molecular sputtering data base of similar scope will provide additional insight into the analytic discrepancies of low-energy sputtering.

The results of these simulations can be compared with the experimental results of Bader, et. al., [44].

Andersen and Bay suggest that non-linear yield enhancement is a slowly decreasing function of energy [39]. The trends of the $0\frac{1}{2}/20^+$ yield ratios at these low energies will be instructive.

Note that the heat of sublimation of copper is 3.53 eV/atom and the surface binding energy is 2.45 eV/atom for the potential functions set into the model [37]. Assume that the incident ions (QRAD) and molecules (QMOL) deposit all their energy into the crystal. The resulting energy per atom values will bracket the heat of sublimation and surface binding energy values. Systematic effects of the relative magnitudes of the energy density, and the surface binding energy and heat of sublimation in the context of the spike model [42] can be studied.

G. POTENTIAL FUNCTIONS

1. Atom-Atom potential functions

The program uses the Pot-II potential function, a compound function which provides a repulsive Born-Mayer (Gibson-2) "wall joined smoothly to an attractive Morse "well" by a cubic spline at the points $R_A = 0.83$ LU and $R_B = 1.10$ LU. See figure 8.

The repulsive wall dominates the collision cascade dynamics. Attractive forces have little effect upon the dynamics but dominate the atom's ability to escape the surface.

The potential function well depth reproduces the solid's heat of sublimation (total energy) by summing ever all possible pairwise interactions. The Cu-Cu potential includes only nearest neighbor and next-nearest neighbor interactions because it is truncated at a radius $R_C = 2.40$ LU. The well also reproduces the solid's static surface binding energy (SBE) at its pre-trajectory level. The SBE is the attraction a sput must overcome. The values of the heat of sublimation and SBE are 3.53 eV/atom and 2.45 eV/atom, respectively.

See reference [38] for a detailed discussion of the atom-atom potential function.

2. Ion-Atom Potential Function

The Cu/O⁺ ion-atom potential function is a compound function consisting of a 0.7-Moliere wall splined to a Morse well at $R_A = 0.44$ LU and $R_B = 0.55$ LU,

Refer to reference [37] for a detailed discussion of the ion-atom potential function.

3. Ion-Ion Potential Function

The oxygen molecule potential function is a Morse potential truncated at $R_C = 2.40$ LU (Fig. 8).

IV. DISCUSSION AND RESULTS

A. ENERGY DISTRIBUTIONS

The characteristics of the sputtered atom energy distributions for the incident energies of 0.5, 1.25, 2.5, and 5.0 kev/ion are compared for the following simulations: (1) QRAD, (2) random molecule, QMOL(R), and (3) longitudinally polarized molecule, QMOL(LP). These distributions are equivalent to those which would be obtained from an ideal experiment which bombards a clean, monocrystalline (111) copper surface in a perfect vacuum, and collects and analyzes each sputtered atom.

1. Normalized Energy Distributions, 0-20 ev/atom

Figures 9-12 are normalized energy distribution curves comparing QRAD, QMOL(R), and QMOL(LP) for each incident energy and a sputtered atom energy range of 0-20 ev/atom. These curves were obtained from total sputtered atom populations of 700-1800 atoms and are plotted as raw data. Individual sputtered atom populations are indicated with each distribution. These small populations produce distributions with many structural details which are not statistically significant. The smooth curves fitted to the data have no physical significance for any of the distributions taken alone. However, when viewed in a series, certain structural trends may be elucidated for

specific simulations at different incident energies or different simulations at a specific energy. Several features of the distributions are strikingly apparent. The maxima occur at precisely the same energy, approximately 1.8 ev/atom. The only exception is the maximum for QRAD at 0.5 kev/ion. However, its maximum at approximately 2.2 ev/atom is within the statistical uncertainty of the simulation and the difference represents a fluctuation of 8-9 sputtered atoms.

A shoulder appears in each distribution between 2 and 5 ev/atom. The shoulders for QRAD and QMOL(LP) decrease in energy and increase in fraction of total yield as incident energy increases. The shoulders for QMOL(R) remain nearly constant as incident energy increases: The widths of the shoulders are 1-1.5 ev/atom and the yield fractions are 0.040-0.054. This is equivalent to a yield fluctuation of 41-95 sputtered atoms. Secondary shoulders may be present in the 6-10 ev/atom range as well as valid structure at higher energies, but the populations are insufficient to define additional features.

2. Normalized Energy Distributions, 0-3 ev/atom

It is instructive to study the normalized energy distributions for the sputtered atom energy range containing the peaks seen in the preceding section. Figures 13-16 are distributions for the energy range 0-3 ev/atom. These distributions are plotted from a "sliding-4"

average of the raw data as follows: raw data points 1-4 are summed, followed by points 2-5, 3-6, 4-7, etc. The set of averaged points is normalized and plotted as the fraction of total yield vs. energy per sputtered atom. As before, the smooth curves fitted to the data have no individual physical significance.

The relative locations of the apparent maxima of the distributions are consistently skewed toward lower energies as indicated by lines A in the figures. Significant shifts of the distributions for a particular simulation as a function of incident energy are not seen. In fact, the constant energy peaks of figures 9-12 suggest that no significant shifts should occur in the 0-3 eV/atom range.

Several apparent peaks are seen in the distributions. Consider the QRAD distributions. The peaks are fitted credibly because of their consistency as the incident ion energy increases. The peak vanishes at 5.0 keV/ion, but note that the total sputtered atom population at 5.0 keV/ion is only half of the populations at the lower incident energies. The 5.0 keV/ion QRAD simulation consists of 1352 trajectories. Nearly 3000 trajectories are necessary to produce a sputtered atom population sufficiently large to verify a peak. No comparable peak behavior is seen for QMOL(R) or QMOL(LP).

Several low-energy shoulders may be real and verifiable for significantly increased populations.

Assume that these structural features are real. Individual sets of trajectories isolating the atoms comprising the features can be studied to: (1) identify the sputtering mechanism generating the QRAD peaks and shoulders, and (2) elucidate the molecular effects responsible for breaking up or reinforcing the mechanisms.

3. Incident Energy Dependence of the Normalized Energy Distributions

Figures 17-22 show the ion/molecule energy dependence of the normalized energy distribution functions for each simulation. The distributions are identical to those previously studied and are displaced vertically along an incident energy scale. Fraction of total yield cannot be read from this scale but an increment of fractional yield is indicated for each figure.

The 0-20 eV/atom distributions, figures 17-19, clearly show the alignment of the peaks and the shifts in shoulder positions. The QRAD shoulders shift linearly to lower energy and higher fraction as incident energy increases. The QMOL(R) shoulders remain constant in energy with no significant shift in yield fraction. The QMOL(LP) shoulders show a non-linear shift to lower energy and higher fraction.

Figures 20-22 are the 0-3 ev/atom distributions. The QRAD peaks remain in the vicinity of 2 ev/atom. The prospective location of a peak in the 5.0 kev/ion distribution, discussed in the preceding section, is clear in figure 20. No significant trends in fine structure are evident in the QMOL(R) or QMOL(LP) distributions. Real shifts in the distributions for either simulation, as a function of incident energy, are not supported.

4. Cumulative Energy Distribution Functions

Figures 23-25 are the cumulative energy distribution functions (CDF) which plot the fraction of sputtered atoms with energy greater than the indicated energy as a function of sputtered atom energy for the range 0-200 ev/atom. The figures compare the simulations as follows: (1) Fig. 23, QRAD vs. QMOL(R), (2) Fig. 24, QRAD vs. QMOL(LP), and (3) Fig. 25, QMOL(R) vs. QMOL(LP). The incident ion energy is indicated with each curve. Note that for a specific incident ion energy the lower of the two curves shows a shift to the low energy region of the range since each plotted point represents the fraction greater than the energy indicated.

Figure 25 shows the only consistent trend for the distributions. The QMOL(R) sputtered atom populations are shifted to lower energies than those for QMOL(LP).

Figure 23 will be particularly instructive in correlating the angular distribution effects discussed in the following section.

B. ANGULAR DISTRIBUTIONS

Figures 26-29 are the angular distributions of sputtered atoms (spot patterns) for QRAD and QMOL(R). These figures are equivalent to spot patterns obtained experimentally by collecting sputtered deposits on flat glass plates.

The most obvious feature of the spot patterns is the six-fold symmetry which has been shown experimentally [14] to be a characteristic of preferential ejection from the (111) surface. The diffuse distribution between the six-fold axes is caused by low-energy (<20 eV) sputtered atoms ejected late in the trajectories when extensive surface disruption has broken down the preferred ejection mechanisms [47].

The density of the spot patterns is directly related to the sputtered atom population. However, there are no consistent trends for QRAD vs. QMOL(R) as a function of incident energy. The QMOL(R) spot patterns are not always "darker" or more diffuse than the corresponding QRAD spot patterns.

The relative densities of the spot patterns for QRAD and QMOL(R) for each incident energy can be correlated to

figure 23, the CDF for QRAD vs. QMOL(R). Consider the 0-20 eV/atom energy range for each incident energy.

1. 0.5 keV/ion

The six-fold axes for QRAD in figure 26a are very well defined but the spot pattern for QMOL(R), figure 26b, is heavily filled between the axes. Figure 23a shows that the CDF for QMOL(R) is shifted more toward lower energies than for QRAD. The higher fraction of low-energy sputtered atoms is responsible for the heavy, diffuse distribution between the axes.

2. 1.25 keV/ion

The CDF for 1.25 keV/ion incident energy, figure 23b, is exactly opposite that for 0.5 keV/ion but the differences in fraction are not as great. This is reflected in the spot patterns, figures 27a and 27b. Each is very dark but the QRAD pattern now shows slightly more filling between the axes than the QMOL(R) pattern.

3. 2.50 keV/ion

The CDF and spot patterns for 2.50 keV/ion incident energy, figures 23c and 28, respectively, follow the same trend as those for 1.25 keV/ion incident energy. The fractional differences in the CDF are smaller but the higher QRAD sputtered atom population produces a darker spot pattern (the percentage difference in sputtered atom population between QRAD and QMOL(R) is greatest at this incident energy).

4. 5.0 kev/ion

The CDF curves for 5.0 kev/ion incident energy, figure 23d, are virtually identical, and the spot patterns for this energy, figures 29a and 29b, are nearly indistinguishable.

C. SPUTTERING YIELD RATIOS

Figure 30 compares the experimental yield ratios, for the sputtering of polycrystalline copper by N^+ and N_2^+ [44], and the simulation sputtering yield ratios.

The sputtering yield ratio is defined as follows:

$$\text{ratio} = \frac{\text{yield from } X_2^+}{2(\text{yield from } X^+)},$$

where X is the bombarding element. Two sets of simulations, "real" and "artificial", are considered.

1. Experimental

The experimental sputtering yield ratios for N^+ and N_2^+ incident upon polycrystalline copper [44] are plotted in figure 30a and 30b for the incident energy range 0-8 kev/ion. A very good straight-line fit is obtained which shows a slowly increasing yield ratio with increasing incident energy.

2. "Real" Simulations

The sputtering yield ratios for the "real" simulations, QMOL(R) and QMOL(LP), are plotted in figure

30a. The connecting lines have no physical significance. In general, the simulation yield ratios increase much more slowly with incident energy than the experimental values. The ratios for QMOL(LP) are consistently lower than those for QMOL(R) and both dip considerably at 1.25 kev/ion incident energy.

3. "Artificial" Simulations

The sputtering yield ratios for two "artificial" simulations are plotted in figure 30b. In the first case, Ar^+ and Ar_2^+ are substituted for O^+ and O_2^+ but the Cu-O ion-atom potential is retained. Therefore, the mass ratios are changed for QRAD and QMOL(R) from 0.251 and 0.503 for O^+/O_2^+ to 0.628 and 1.257 for $\text{Ar}^+/\text{Ar}_2^+$, respectively. In the second case, the B-potential [37] is substituted for the Cu-O potential and the oxygen mass is retained. The ratios for $\text{Ar}_2^+/\text{Ar}^+$ are lower than the corresponding "real" QMOL(R) ratios in figure 30a and an identical dip occurs at 1.25 kev/ion is almost totally absent.

D. EFFECTS OF MOLECULAR ORIENTATION

The effects of molecular orientation upon the sputtering yield ratio are examined for the following: (1) longitudinally polarized molecule, QMOL(LP), (2) transversely polarized molecule ($\theta_m = 90$ deg.), QMOL(TP) and (3) polar angle $\theta_m = 45$ deg., QMOL(45). Figures 31a

and 31b show the sputtering yield ratio as a function of azimuthal angle, ϕ_m , at 1.25 kev/ion incident energy for QMOL(TP) and QMOL(45). Lines of constant yield ratio are indicated for QMOL(LP) at 1.25 kev/ion incident energy and the average QMOL(LP) yield ratio for the four incident energies. Note that azimuthal angle is not defined for a longitudinally polarized molecule.

1. General

On the average for a random molecular orientation, the two dissociated ions will not collide with the surface simultaneously. When the molecule is transversely polarized, the time separation between collisions is minimized and the separation between impact points is the greatest. The degree of overlap of the individual collision cascades will be determined by the separation in the diatomic molecule, 1.22 Å for O_2 . When the molecule is longitudinally polarized, the time separation is maximized and the impact points are very nearly identical.

The longitudinally polarized molecule produces the highest energy density in the collision cascade since the energy from both ions is deposited in the same region of the lattice. If energy density were the controlling factor, the longitudinally polarized molecule should produce the highest yield ratios.

The trailing ion in the longitudinally polarized molecule is colliding with a surface already disrupted by

the leading ion and, in general, will not "see" a surface layer atom before impact. In addition, the trailing ion overtakes the leading ion and is deflected slightly by the leading ion's collision with the surface. These factors may result in increased penetration depths and a higher incidence of channeling for bombardment by longitudinally polarized molecules.

2. Yield Ratios

The yield ratios for QMOL(LP) and QMOL(45) at 1.25 kev/ion incident energy are plotted in figure 31, with QMOL(LP) yield ratios indicated, as a function of the azimuthal angle ϕ_m . The ratios for both cases show a good linear fit and are nearly identical. The QMOL(LP) values are not significantly different from either QMOL(TP) or QMOL(45).

3. Scattered ions

The following table summarizes and compares total yields and the number of scattered ions for QRAD, QMOL(R) and QMOL(LP):

		no. traj	total yield	scattered ions
0.5 kev/ion	QRAD	936	1665	104
	QMOL(R)	520	1770	225
	QMOL(LP)	520	1657	138
1.25 kev/ion	QRAD	936	1653	72
	QMOL(R)	520	1660	67
	QMOL(LP)	520	1437	42
2.50 kev/ion	QRAD	1352	1439	20
	QMOL(R)	520	1181	29
	QMOL(LP)	520	1069	15
5.0 kev/ion	QRAD	1352	927	8
	QMOL(R)	520	760	6
	QMOL(LP)	520	746	2

E. OTHER MOLECULAR EFFECTS

1. Yield per Layer

Detailed analyses of single-ion sputtering trajectories have shown that the majority of sputtered atoms come from sputtering mechanisms which are completely confined to the surface and near-surface layers [29]. Consequently, the majority of sputtered atoms come from the surface layer.

The sputtering yields for each layer of the microcrystal are listed below, for each simulation and incident energy, with the fractional yields from layer 2 (L_2/N) and all subsurface layers $((L_2 + L_3 + L_4)/N)$ indicated.

0.5 kev/ion	Total yield, N	# Each Layer L1/L2/L3/L4	$\frac{L_2}{N}$	$\frac{L_2+L_3+L_4}{N}$
QRAD	1665	1635/28/2/0	0.016	0.018
QMOL(R)	1770	1708/53/7/2	0.029	0.035
QMOL(LP)	1657	1589/54/13/1	0.032	0.041
1.25 kev/ion				
QRAD	1653	1626/23/2/2	0.013	0.016
QMOL(R)	1660	1614/31/15/0	0.018	0.027
QMOL(LP)	1437	1397/35/5/0	0.024	0.027
2.50 kev/ion				
QRAD	1439	1420/16/3/0	0.011	0.013
QMOL(R)	1181	1147/31/3/0	0.026	0.028
QMOL(LP)	1069	1033/35/1/0	0.032	0.033
5.0 kev/ion				
QRAD	927	909/17/1/0	0.018	0.019
QMOL(R)	760	737/21/2/0	0.027	0.030
QMOL(LP)	746	718/26/2/0	0.034	0.037

Note that for molecular sputtering, the vast majority of sputtered atoms still originate in the surface layer. However, the relative yields from subsurface layers are much greater for molecular than for single-ion sputtering.

2. Normalized Sputtering Frequency

Figures 32-39 are the surface layer sputtering frequency-location diagrams for QRAD and QMOL(R) at each incident energy. Each diagram is normalized to the most frequently sputtered atom for the simulation: a circle containing ten rings indicates the most frequently sputtered atom(s). A circle containing zero rings is an atom that never sputtered and one ring indicates an atom that sputtered at least once in the entire set of trajectories.

Atom 43 (44), for QRAD (QMOL), is the primary knock-on atom (PKA) in at least 46% of the trajectories (see figure 5). It is always one of the least sputtered atoms. In fact, its frequency decreases as incident energy increases. Note that the PKA sputtering frequencies are always equal for QRAD and QMOL(R) at each incident energy, with the exception of 2.50 kev/ion: at this energy the frequencies differ by less than 0.1.

At 0.5 kev/ion, the most frequently sputtered atoms are both nearest and next-nearest neighbors, relative to the PKA. But at 1.25, 2.5, and 5.0 kev/ion the most frequently sputtered atoms are almost exclusively next to

the most frequently sputtered atoms are triangular or diamond-shaped.

F. THE MODEL

Computer run-times for QMOL are, on the average, nearly twice those for QRAD at the same energy per incident ion. This is reasonable since a QMOL simulation is essentially a superposition of two single-ion collision cascades. Run-time increases as incident energy decreases because of ion size effects. Several QMOL simulations, particularly at 0.50 kev/ion, had to be split into two separate runs to avoid exceeding the computer system's job time constraints.

The reproducibility of a QMOL trajectory is extremely sensitive to the precision of θ_m and ϕ_m . The IBM 360 system is designed to retain 7 significant digits, in single-precision, and this is the precision of the random angles θ_m and ϕ_m . An attempt to reconstruct a trajectory by manually entering θ_m and ϕ_m to 3 significant digits produced only 2 of the original 10 sputtered atoms for the trajectory. Subsequent entries of 4 and 5 significant digits produced yields of 4 and 7 sputtered atoms, respectively. The reconstruction loop reproduces a trajectory exactly.

V. CONCLUSIONS

A. THE MODEL

This research reinforces the feasibility and flexibility of computer simulated sputtering. The single-ion sputtering model was easily modified to simulate homonuclear, diatomic molecular sputtering within the original constraints and basic physical assumptions. No additional approximations or rethinking of the physics inherent in the basic model were necessary.

B. SPUTTERED ATOM NORMALIZED ENERGY DISTRIBUTIONS

Recall the alignment of the peaks in the 0-20 ev/sputtered atom distributions. The peaks are clearly not an incident energy, energy density, or molecular orientation effect. Preliminary results of other simulations, not included here, show that the peaks are insensitive to the mass ratio, but do shift to lower energies when the ion-atom potential function is changed from the Cu- O^+ compound potential to the B-potential. The shift is nearly identical for single-ion and molecular sputtering.

The 0-3 ev/sputtered atom energy distributions provide the greatest insight into the effects of the molecule upon the sputtering process. The QRAD peaks for 0.50, 1.25, and 2.50 kev/ion incident energy may be real. A mechanism unique to the QMOL cascades is clearly breaking up the

peaks and in one case (QMOL(R) at 2.50 kev/ion) may be reinforcing the peak. The source of this molecular sputtering mechanism may be linked to the substantially increased fraction of sputtered atoms from subsurface layers for the QMOL simulations.

C. YIELD RATIOS

The simulation sputtering yield ratios agree reasonably well with experimental data. Two primary factors may cause the differences in yield ratios: (1) the difference in ion-atom potential functions, and (2) the polycrystalline target used in the laboratory experiments. Mass ratio is probably not significant since the mass ratios for N and O differ by only 12%.

The majority of the yield ratios are less than one and, in general, the overall trend for the yield ratios is a slow increase with increasing incident energy. Energy density is not an accurate predictor of the sputtering yield ratio. In fact, the yield ratios for the longitudinally polarized molecule, the configuration producing the highest energy density in the lattice, are all lower than the ratios for the corresponding random molecule simulations.

The anomalous dip in the sputtering yield ratios at 1.25 kev/ion may be an artifact of the ion-atom potential

function since it vanishes in the B-potential "artificial" simulation. It is interesting to note that 1.25 kev averaged over the 360 - atom microcrystal is only 0.06 ev/atom less than the heat of sublimation of the microcrystal modelled by the Cu-Cu potential function.

D. MOLECULAR ORIENTATION

Sputtering yield ratio is strikingly insensitive to molecular orientation at 1.25 kev/ion incident energy. Although QMOL(TP) and QMOL(45) yield ratios are not available for the other incident energies, no significant difference is expected since the QMOL(R) and QMOL(LP) ratios are close at those energies.

Molecular beam polarizability may have a definite application for ion implantation. The QMOL(LP) simulations produced substantially less scattered incident ions at 1.25, 2.5, and 5.0 kev/ion.

VI. RECOMMENDATIONS

A. THE MODEL

QMOL can easily be modified to simulate sputtering by an AB-type molecule as follows. Change the random number generator loop to produce six random numbers instead of five. Use the sixth random number to set $0 < \theta_m \leq \pi$ or $\pi < \theta_m \leq 2\pi$ in the same way that the fifth random number sets the value of ϕ_m . The atom that is in the lower hemisphere of the molecule's locus of orientation becomes ion(1). The program then sets up the molecule at the impact point. In principle, the program can be modified to simulate sputtering by triatomic or higher-order polyatomic molecules.

B. SPUTTERED ATOM NORMALIZED ENERGY DISTRIBUTIONS

It is necessary to identify specific atoms comprising the QRAD peaks. Then, individual QMOL trajectories common to these atoms can be examined in detail to elucidate how a peak is dispersed into a much wider energy band. However, sputtered atom populations for QRAD at 5.0 kev/ion and all QMOL simulations are too sparse and statistically uncertain for this detailed analysis. The 5.0 kev/ion QRAD simulation should be run with a new displaced data set designed to augment the 1352 trajectories already executed

and produce a sputtered atom population sufficiently large to confirm or negate the appearance of a peak. Likewise, each QMOL sputtered atom population should be augmented by runs with the displaced data set no. 2 impact points. The combination of much larger sputtered atom populations and the sliding-4 averaging technique will enable more precise correlation between structural features in the 0-3 ev/sputtered atom energy distributions.

C. YIELD RATIOS

A systematic study of the differences between the simulation and experimental sputtering yield ratios must focus upon variations in the ion-atom potential function until laboratory data for single-crystal molecular sputtering becomes available. Two primary options are available: (1) Model the Cu-N⁺ potential while retaining the oxygen mass in the simulation, and (2) increase the O₂ bond length to reduce cascade overlap.

Individual trajectories should be compared for QMOL(R) at 0.50 and 1.25 kev/ion, and QMOL(LP) at 1.25 and 2.50 kev/ion to bracket the dip at its largest variation. The relative positions of the ions for each type of simulation can be traced from timestep to timestep in the individual trajectories. This may show peculiar differences in cascade overlap causing inconsistent yield ratios.

D. ION-ATOM POTENTIAL FUNCTION

The cubic spline in the Cu-O⁺ potential function must be adjusted. A slight knee in the curve occurs at approximately 100 ev potential energy and 0.5 LU separation when the function is plotted from the program's potential table. This shows that the spline is not precisely matching the magnitude and slope of the Moliere and Morse potentials at the current values of $R_A = 0.44$ LU and $R_B = 0.55$ LU. For an initial iteration change R_A and R_B to 0.40 and 0.60 LU, respectively, execute the program for one timestep to print a new potential table, and replot the ion-atom potential function. A change in the spline will not affect the simulation results.

REFERENCES

1. W. R. Grove, Trans. Roy Soc. (London) 142, 87 (1852).
2. R. Behrisch, Ergeb. Exakten Naturwiss. 35, 295 (1964).
3. G. Carter and J. S. Colligon, Ion Bombardment of Solids (American Elsevier Publishing, Inc., New York, 1968).
4. F. M. Penning, J. H. A. Moubis, Koninkl. Ned. Akad. Wetenschap. Proc. 43, 41 (1940).
5. U. A. Arifov, R. R. Rakhimov, and O. V. Khozinskii, Bulletin Acad. Sci. (USSR) Phys. Ser. 26, 1422 (1963).
6. O. C. Yonts and D. E. Harrison, Jr., J. Appl. Phys. 31, 1583 (1960).
7. J. Stark, Die Elektrizitat in Gasen (Barth, Leipzig 1902).
8. J. Stark, Z. Elektrochem. 14, 752 (1908); 15, 509 (1909).
9. K. H. Kingdon, I. Langmuir, Phys. Rev. 20, 107 (1922); 21, 210 (1923); 22, 148 (1923).
10. A. v. Hippel, Ann. Physik 81, 1043 (1926).
11. C. H. Townes, Phys. Rev. 65, 319 (1944).
12. F. Keywell, Phys. Rev. 87, 160 (1952); 97, 1611 (1955).
13. D. E. Harrison, Jr., Phys. Rev. 102, 1473 (1956); 105, 1202 (1957); 32, 1336 (1960).
14. G. K. Wehner, Phys. Rev. 102, 690 (1956).
15. R. H. Silsbee, J. Appl. Phys. 28, 1246 (1957).
16. M. T. Robinson and O. S. Oen, Appl. Phys. Lett. 2, 30 (1963).

17. M. T. Robinson and O. S. Oen, Phys. Rev. 132, 2385 (1963).
18. G. R. Piercy, F. Brown, J. A. Davies, and M. McCargo, Phys. Rev. Lett. 10, 399 (1963).
19. H. Lutz and R. Sizmann, Phys. Lett. 5, 113 (1963).
20. R. S. Nelson and M. W. Thompson, Philos. Mag. 8, 1677 (1963).
21. G. Carter and J. S. Colligon, Ion Bombardment of Solids (American Elsevier Publishing, Inc., New York, 1968), pp. 226-237.
22. P. Sigmund, Phys. Rev. 184, 383 (1969).
23. R. Behrisch, ed., Sputtering by Particle Bombardment I (Springer-Verlag, 1981). chpt. 2.
24. M. W. Thompson, Philos. Mag. 18, 377 (1968).
25. M. T. Robinson, Philos. Mag. 12, 145, 741 (1965).
26. U. Littmark and S. Fedder, Nuc. Inst. and Meth. 194, 607 (1982).
27. J. B. Gibson, A. N. Goland, M. Milgram, and G. H. Vineyard, Phys. Rev. 120, 1229 (1960).
28. W. L. Gay and D. E. Harrison, Jr., Phys. Rev. 135, A1780 (1964).
29. D. E. Harrison, Jr., N. S. Levy, J. P. Johnson, III, and H. M. Effron, J. Appl. Phys. 39, 3742 (1968).
30. D. E. Harrison, Jr., J. Appl. Phys. 40, 3870 (1969).
31. D. E. Harrison, Jr., W. L. Moore, Jr., and H. T. Holcombe, Radiat. Eff. 17, 167 (1973).
32. D. E. Harrison, Jr., and C. B. Delaplain, J. Appl. Phys. 47, 2252 (1976).
33. Chr. Lehmann and P. Sigmund, Phys. Stat. Sol. 16, 507 (1966).
34. D. E. Harrison, Jr., Proc. Symp. Sputtering Venna, ed. by P. Varga, G. Betz, and F. P. Viehbock (Technische Universitat Wien, Austria 1980).

35. D. E. Harrison, Jr., Radiat. Eff. 70, 1 (1983).
36. R. Behrisch, ed., Sputtering by Particle Bombardment I (Springer-Verlag, 1981).
37. D. E. Harrison, Jr., J. Appl. Phys. 52, 1499 (1981).
38. D. E. Harrison, Jr., and R. P. Webb, J. Appl. Phys. 53, 4193 (1982).
39. H. H. Andersen and H. L. Bay, J. Appl. Phys. 45, 953 (1974); 46, 2416 (1975).
40. S. S. Johar and D. A. Thompson, Surf. Sci. 90, 319 (1979).
41. D. A. Thompson and S. S. Johar, Appl. Phys. Lett. 34, 342 (1979).
42. K. L. Merkle and W. Jager, Philos Mag. A. 44, 741 (1981).
43. R. Kelly, Radiat. Eff. 32, 91 (1977).
44. M. Bader, F. C. Witteborn, and T. W. Snouse, NASA TR R-105 (1961).
45. D. E. Harrison, Jr., W. L. Gay, and H. M. Effron, J. Math. Phys. 10, 1179 (1969).
46. K. Foley, Thesis, Purdue Univ., (unpublished), 1981.
47. N. Winograd, B.J. Garrison, and D.E. Harrison, Jr., Phys. Rev. Lett. 41, 1120 (1978).

Cu (FCC) Microcrystal
 (15 x 4 x 12)
 360 atoms

See text for definitions
 of indicated dimensions.

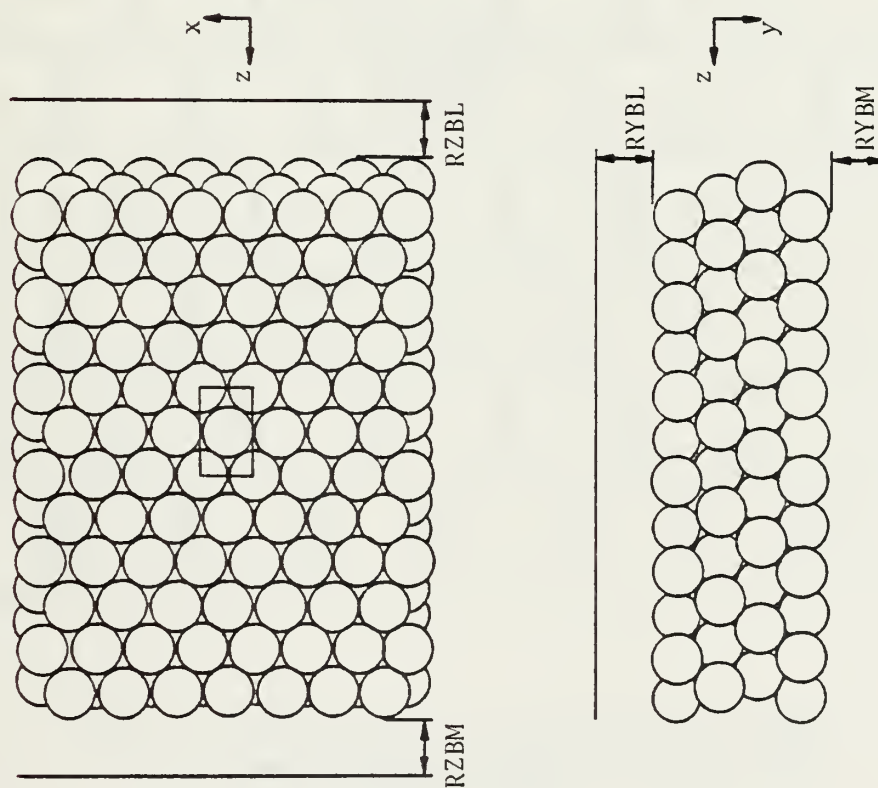


Fig. 1. 3-view drawing of the microcrystal.

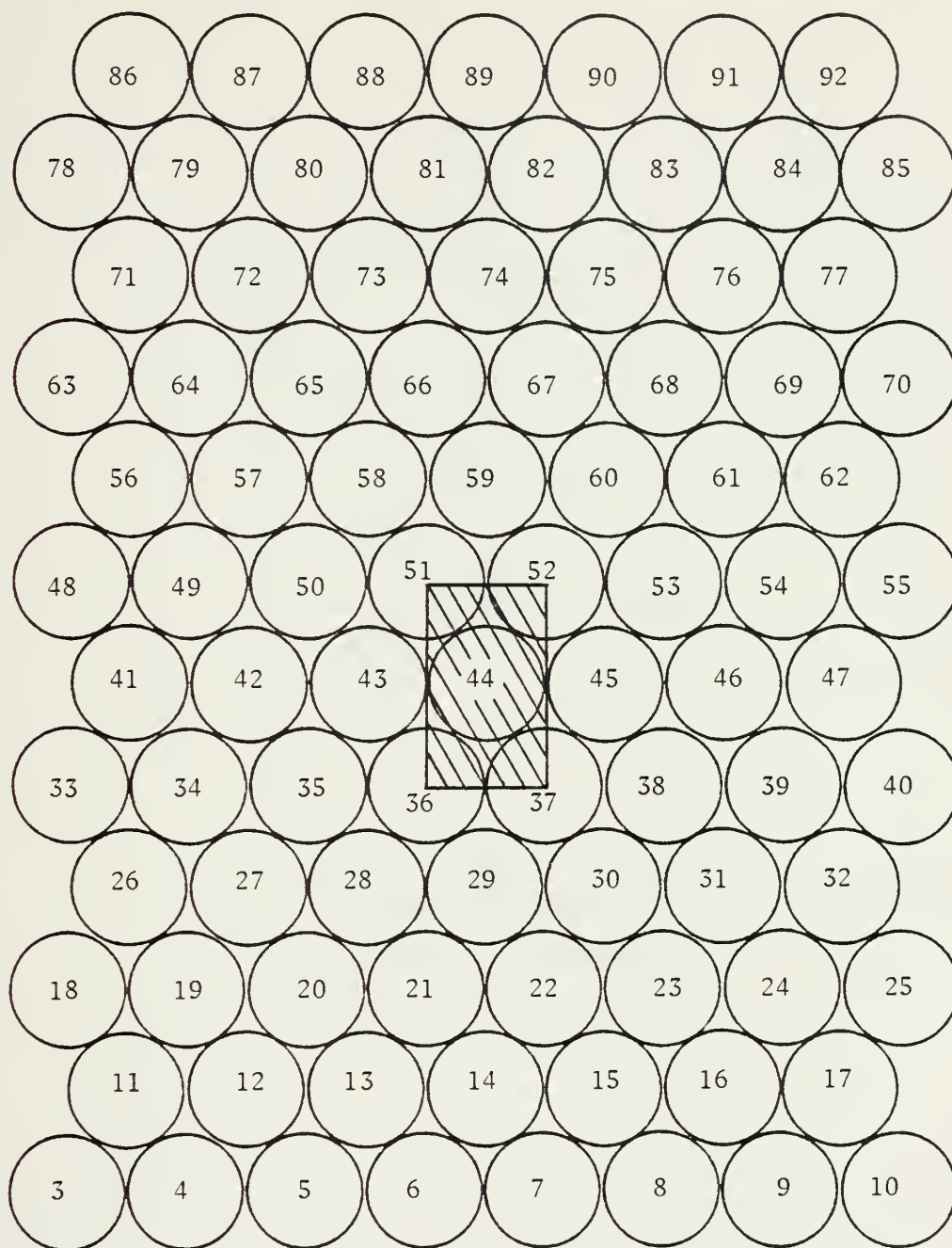


Fig. 2. Microcrystal surface layer and impact area. Note that the atom numbers are for the program QMOL.

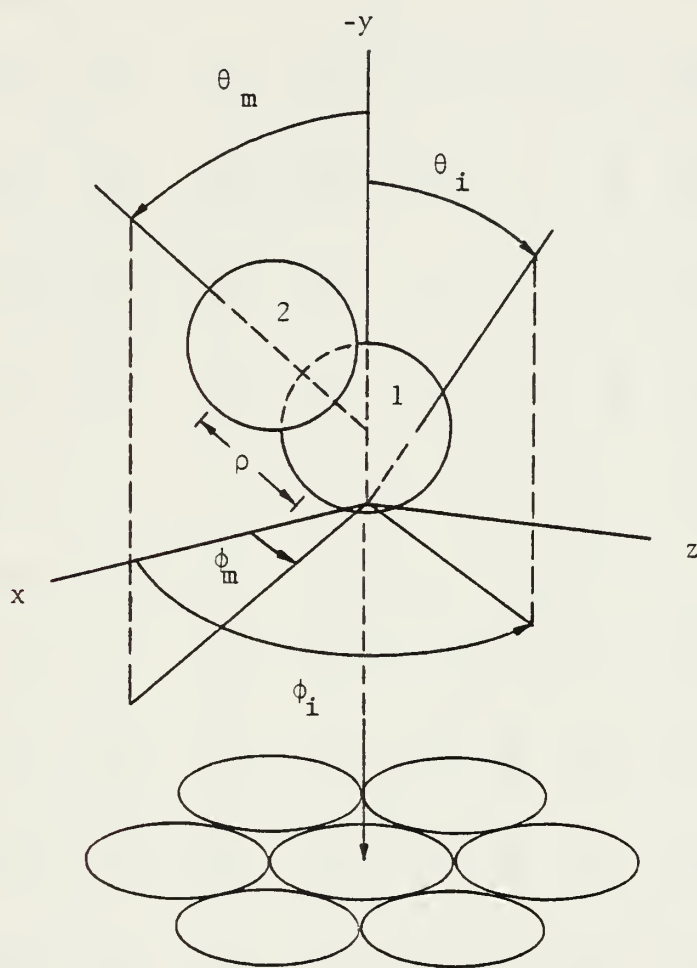


Fig. 3. Molecule orientation with respect to the (111) surface of the target.

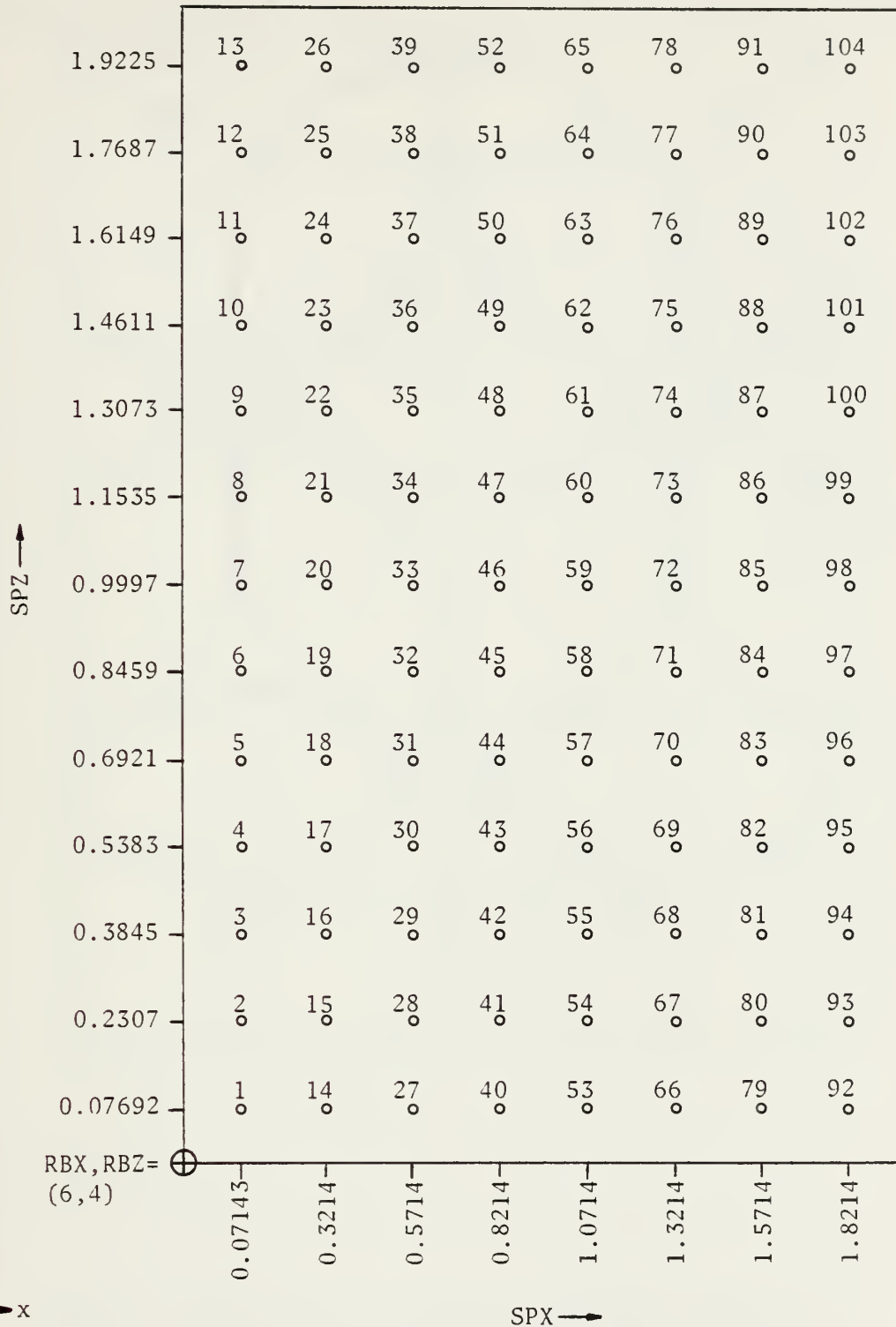


Fig. 4. Impact area and impact point coordinates. Each impact point is labelled with its corresponding simulation trajectory number.

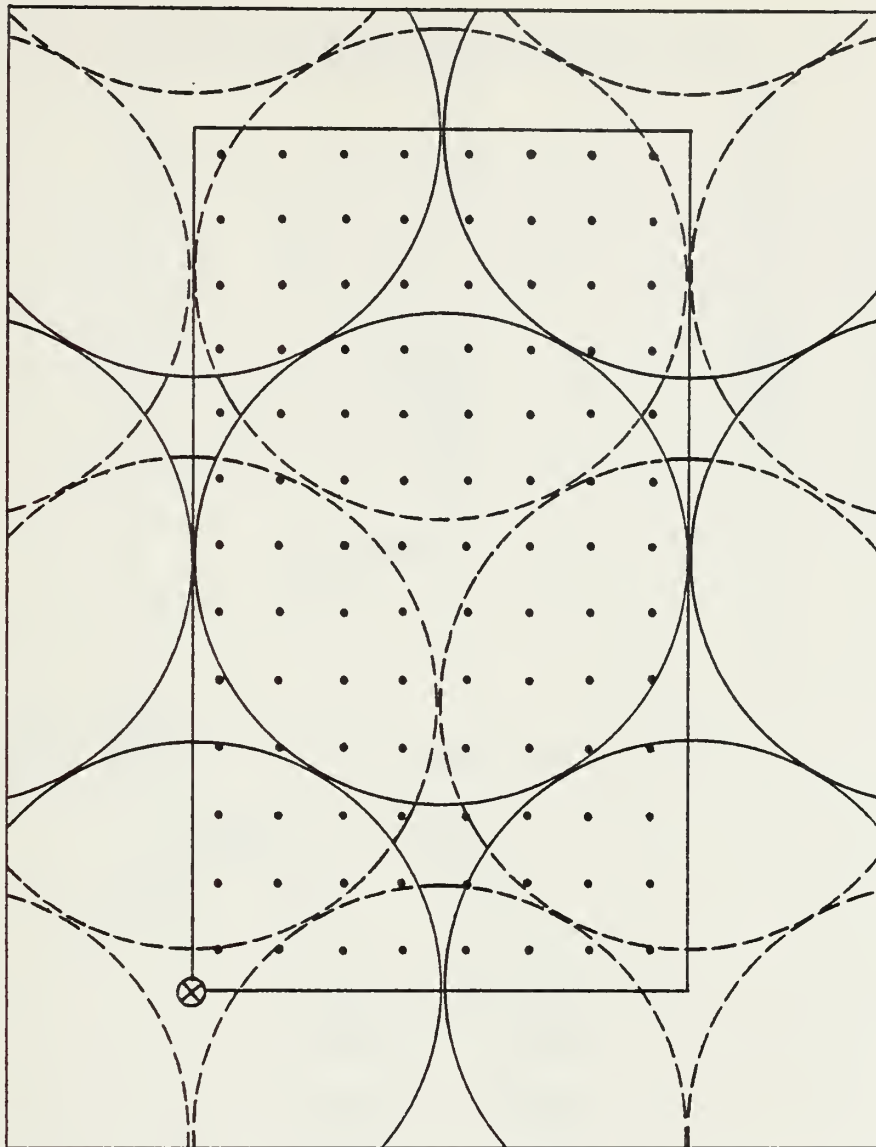
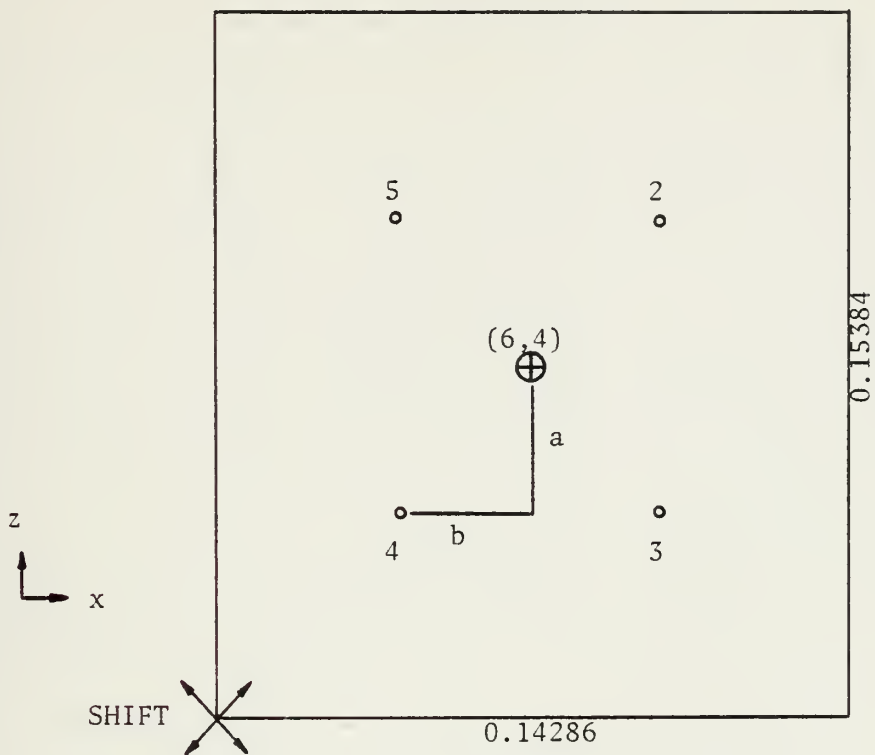


Fig. 5. Impact area on the (111) surface, drawn to scale. The central atom is atom 44 (QMOL). The dashed circles are second-layer atoms.

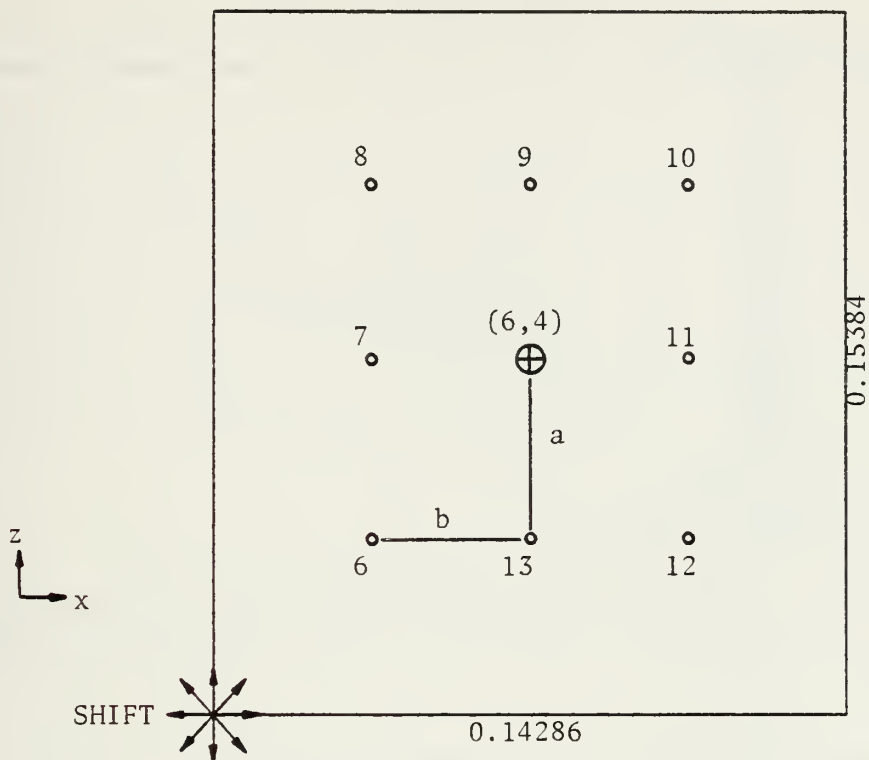


$a = 0.02564$, $b = 0.02381$

POINT	RBX	RBZ
1	6.0000	4.0000
2	6.02381	4.02564
3	6.02381	3.97436
4	5.97619	3.97436
5	5.97619	4.02564

All units are planes.

Fig. 6. Displaced data set no. 1.



$a = 0.03846$, $b = 0.03572$

POINT	RBX	RBZ
6	5.96428	3.96154
7	5.96428	4.00000
8	5.96428	4.03846
9	6.00000	4.03846
10	6.03572	4.03846
11	6.03572	4.00000
12	6.03572	3.96154
13	6.00000	3.96154

All units are planes.

Fig. 7. Displaced data set no. 2.

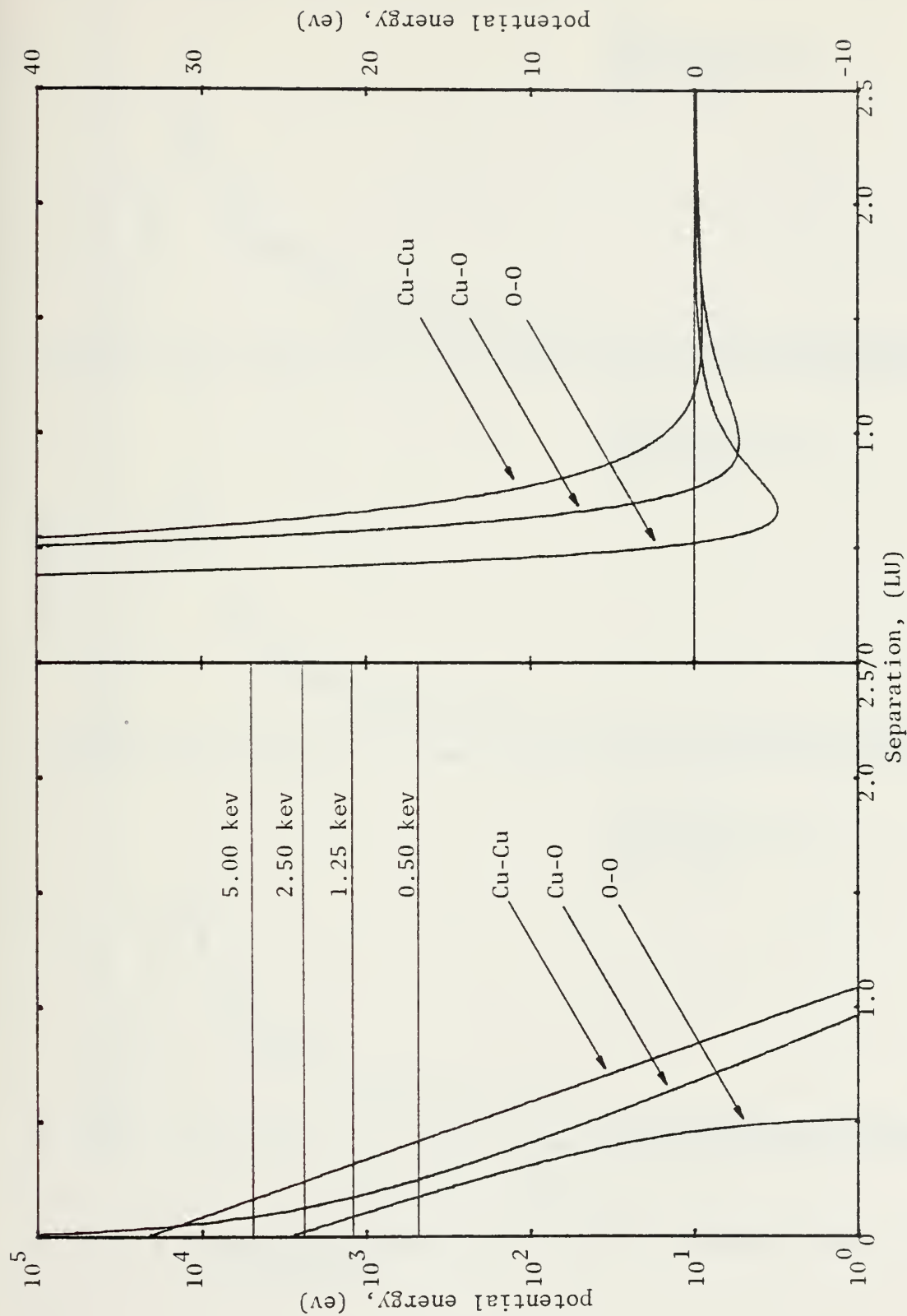


Fig. 8. Interatomic potential functions used in this thesis. The LU (lattice unit) equals 1.8075 Å, one-half the lattice constant for Cu.

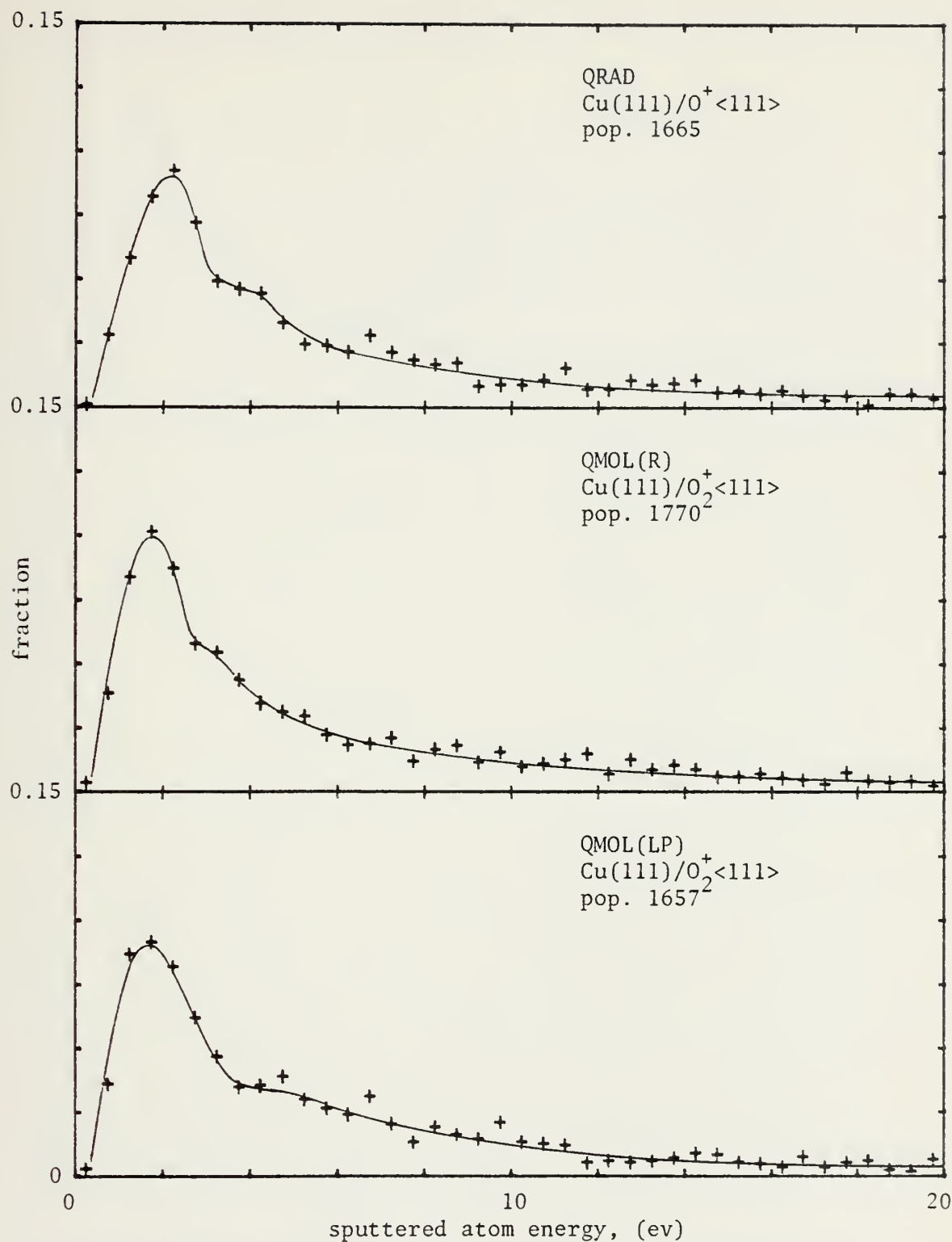


Fig. 9. Normalized energy distribution of sputtered atoms, 0-20 ev, 0.50 kev/ion.

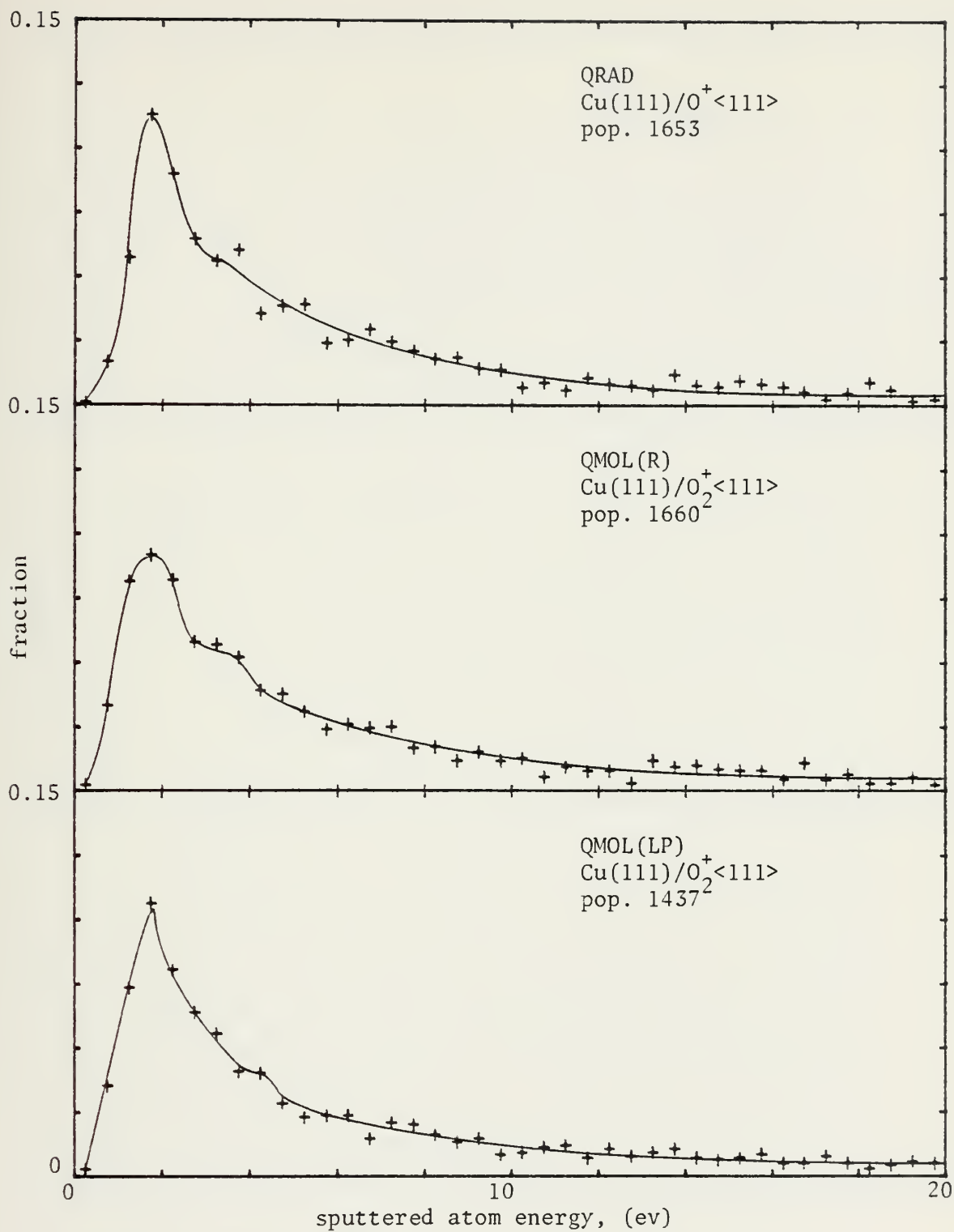


Fig. 10. Normalized energy distribution of sputtered atoms, 0-20 ev, 1.25 kev/ion.

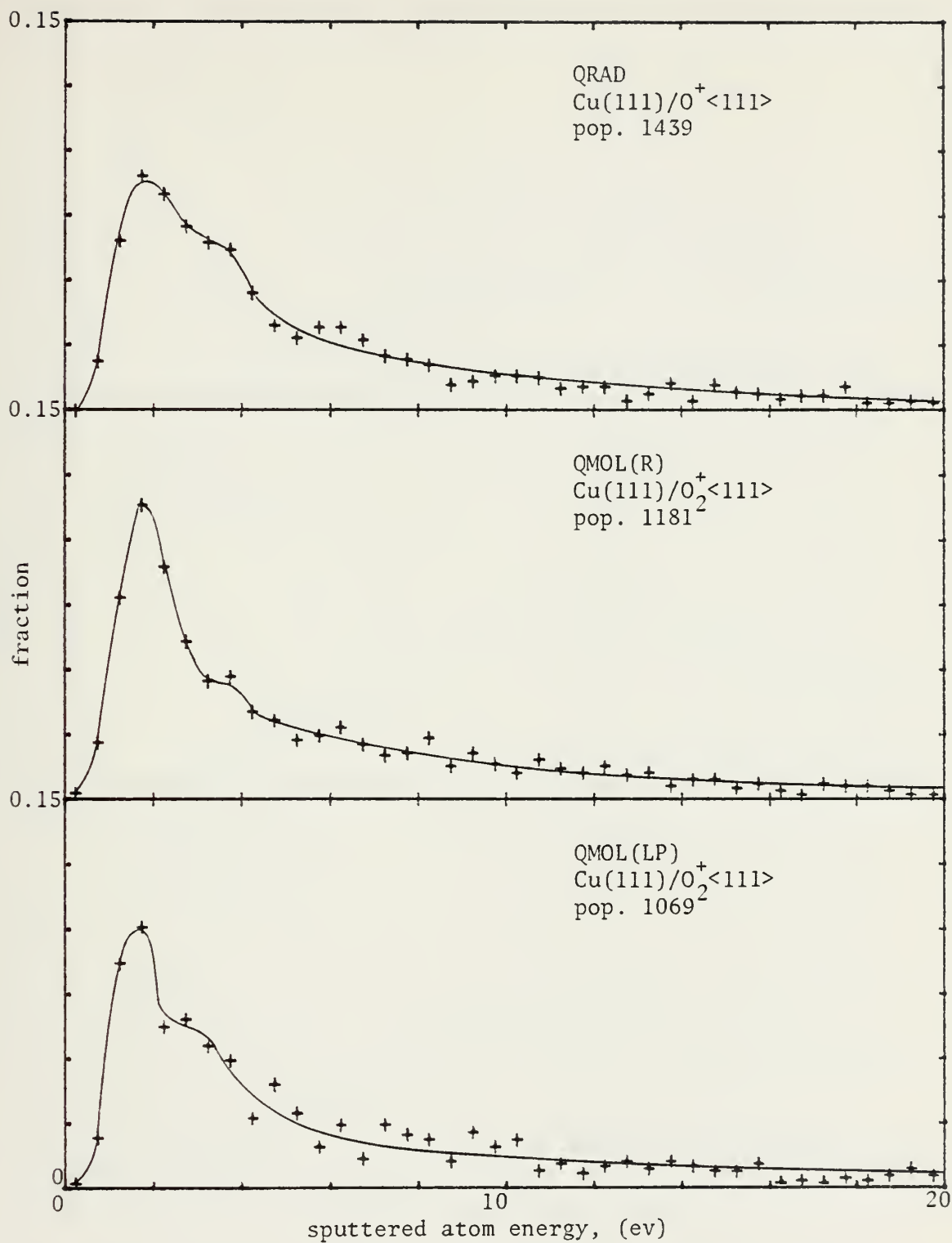


Fig. 11. Normalized energy distribution of sputtered atoms, 0-20 ev, 2.50 kev/ion.

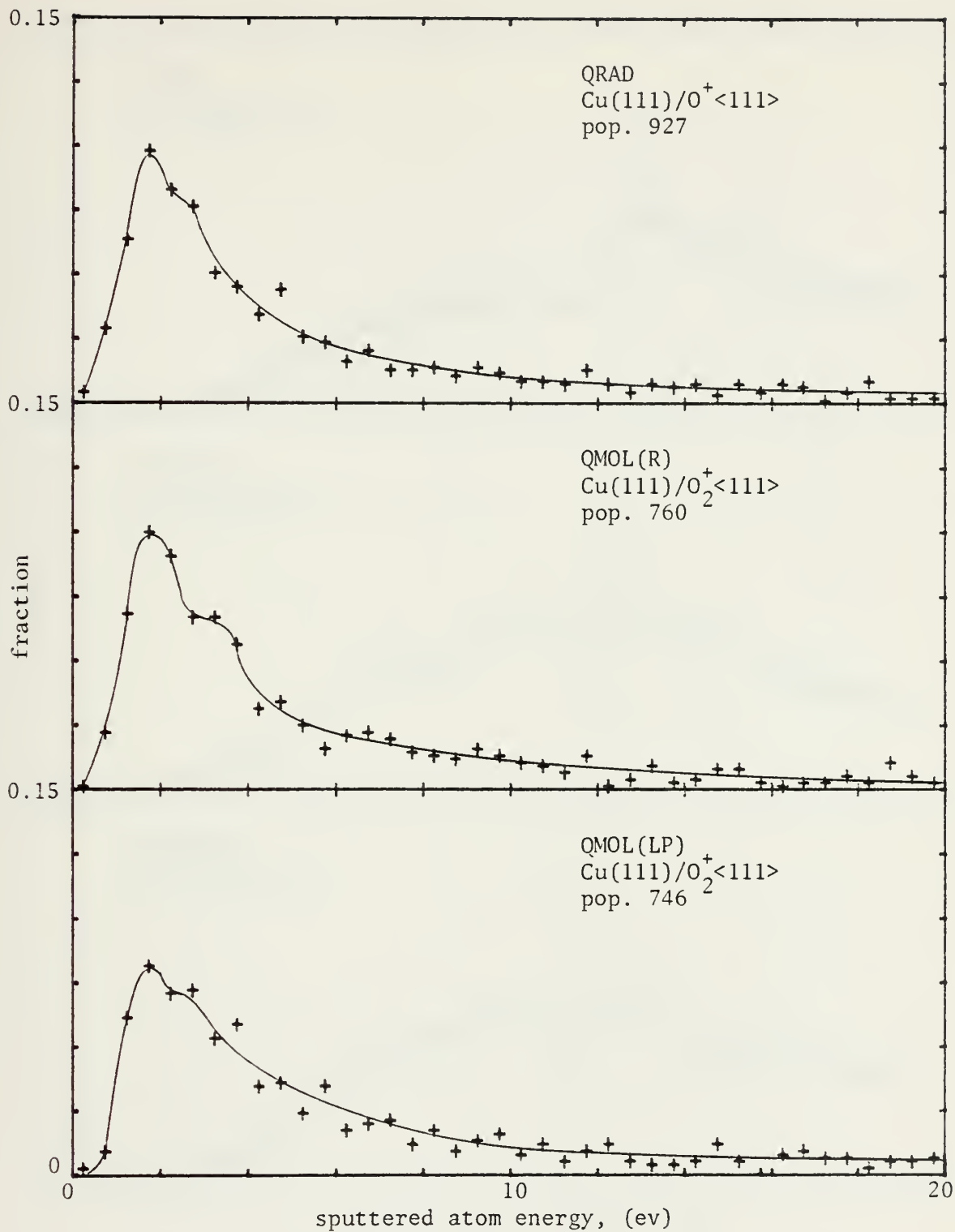


Fig. 12. Normalized energy distribution of sputtered atoms, 0-20 ev, 5.0 kev/ion.

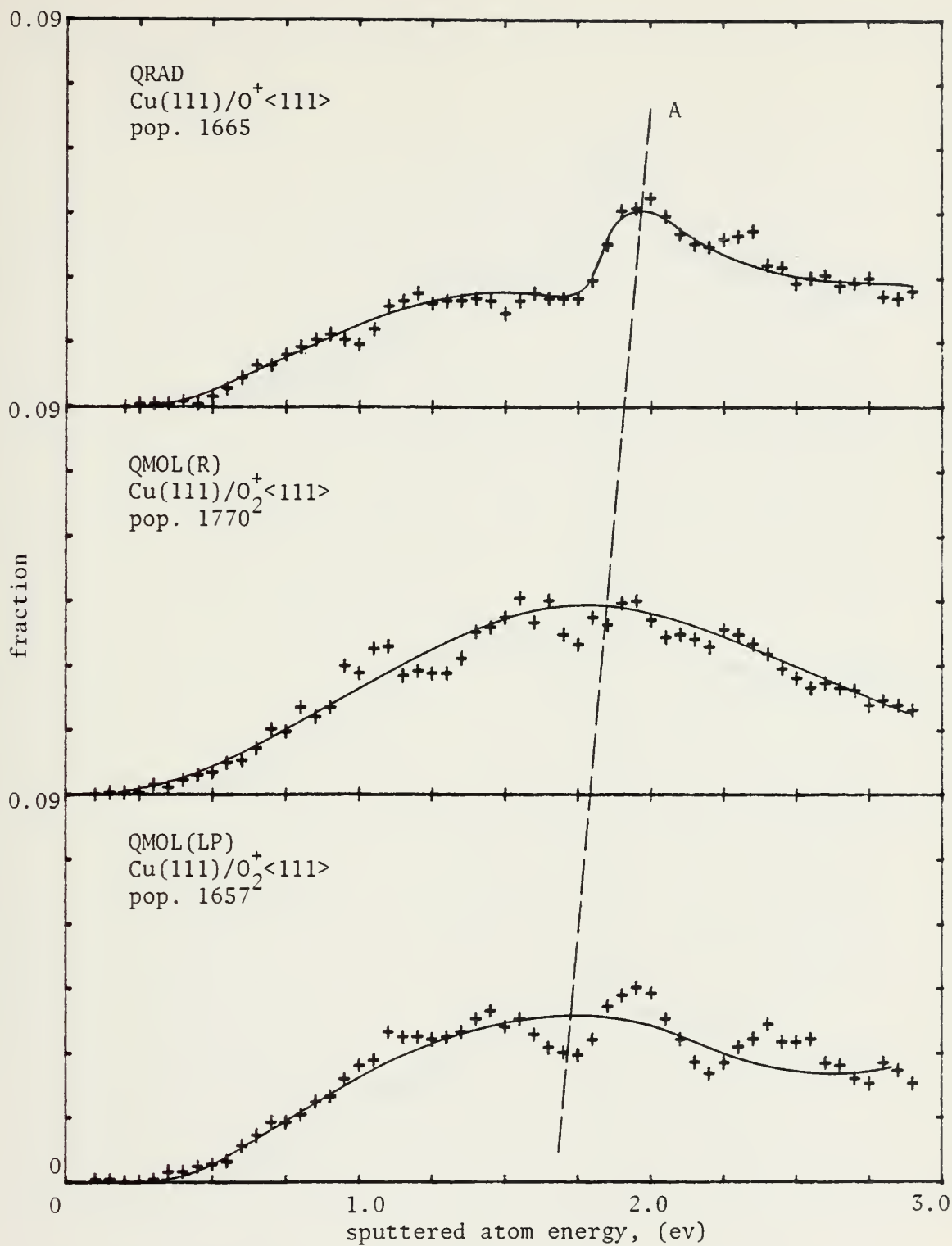


Fig. 13. Normalized energy distribution of sputtered atoms, 0-3 ev, 0.50 kev/ion.

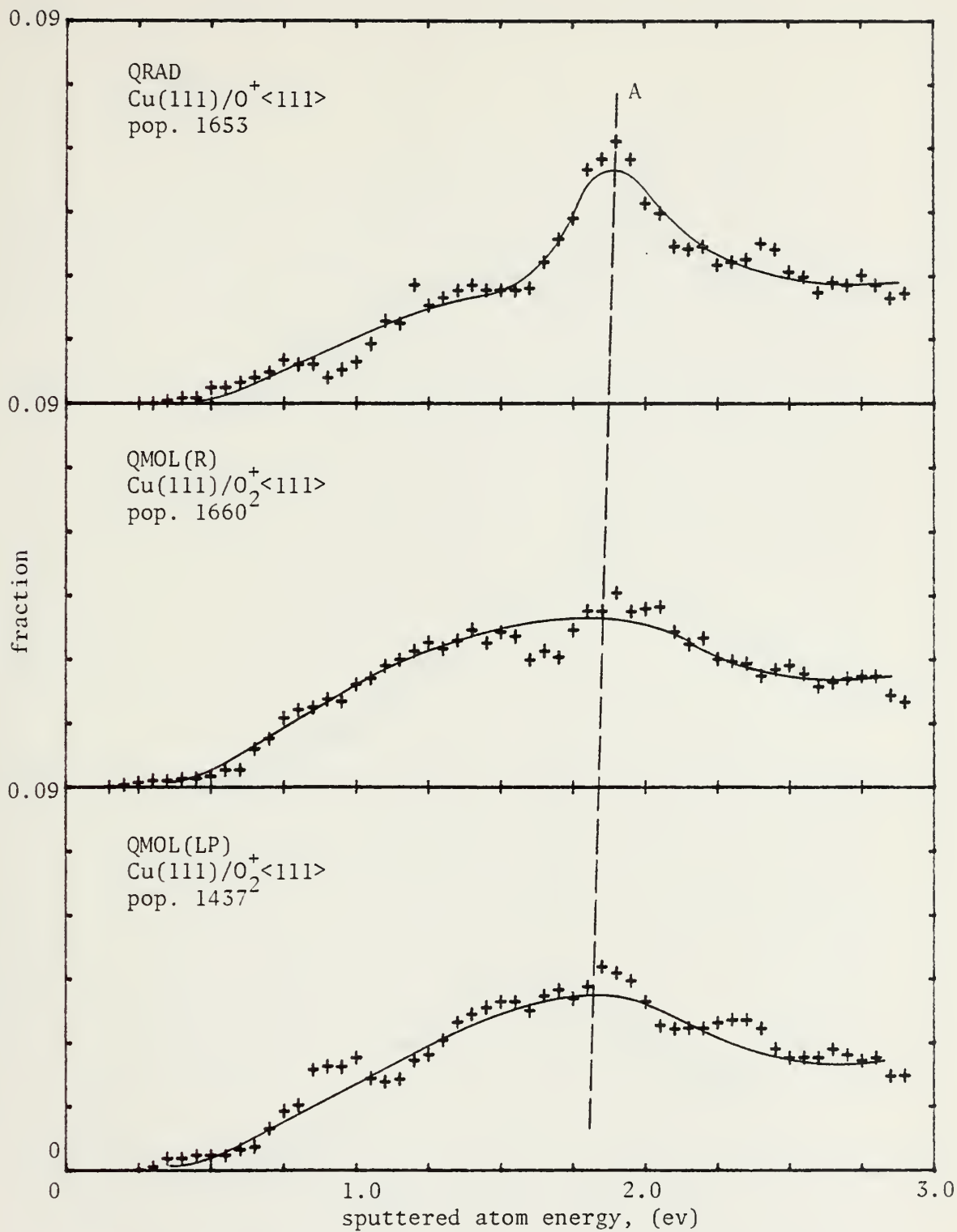


Fig. 14. Normalized energy distribution of sputtered atoms, 0-3 ev, 1.25 kev/ion.

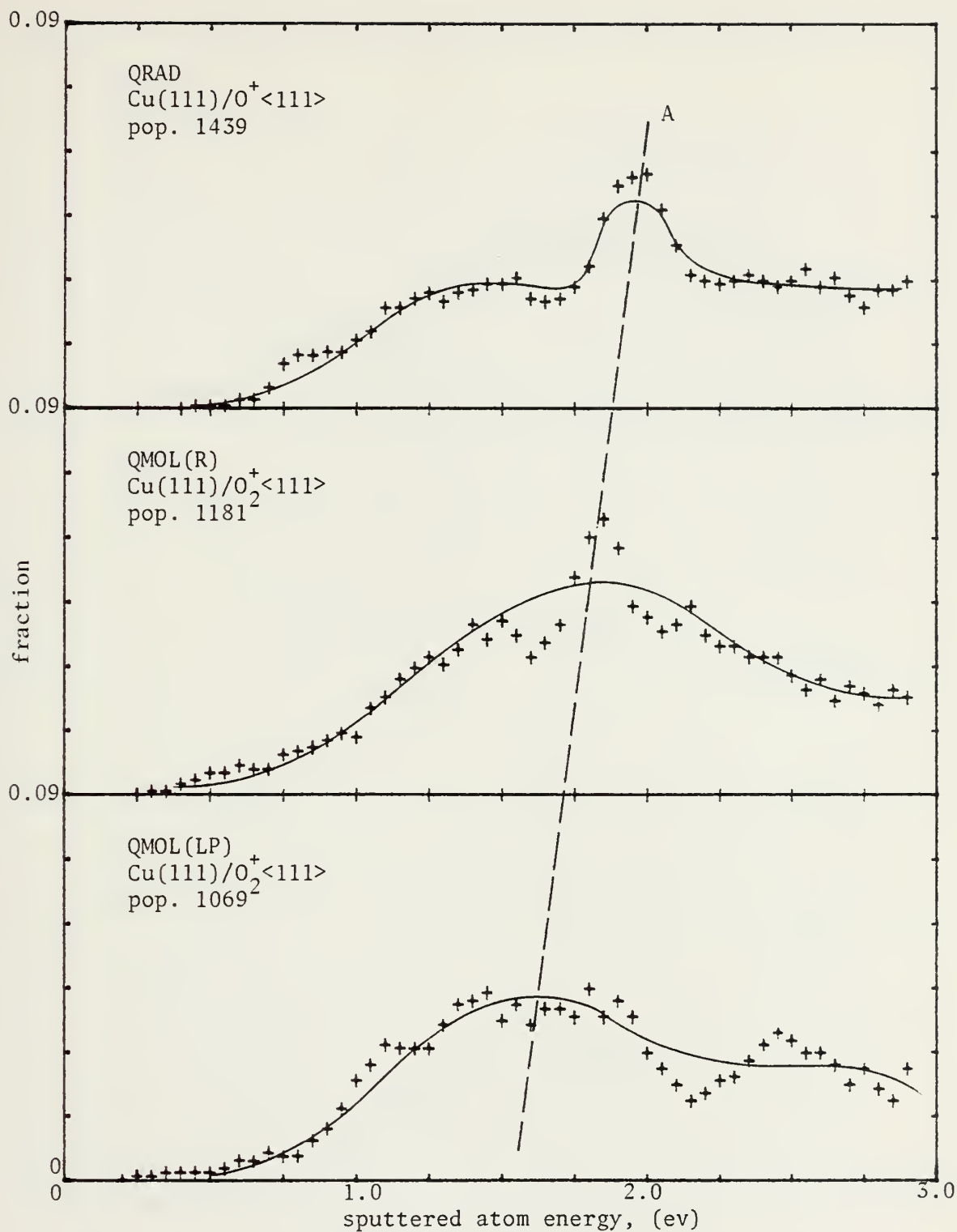


Fig. 15. Normalized energy distribution of sputtered atoms, 0-3 ev, 2.5 kev/ion.

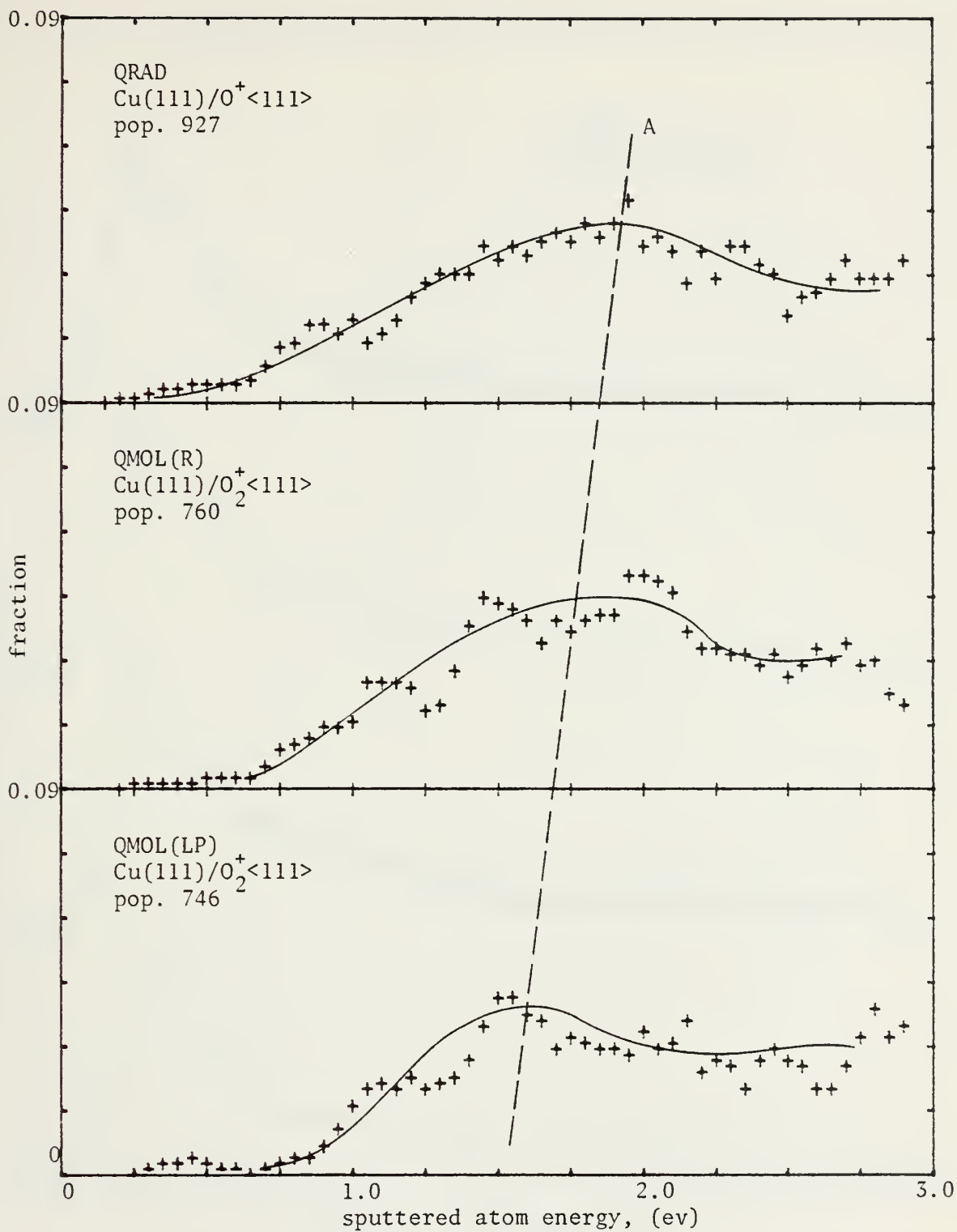


Fig. 16. Normalized energy distribution of sputtered atoms, 0-3 ev, 5.0 kev/ion.

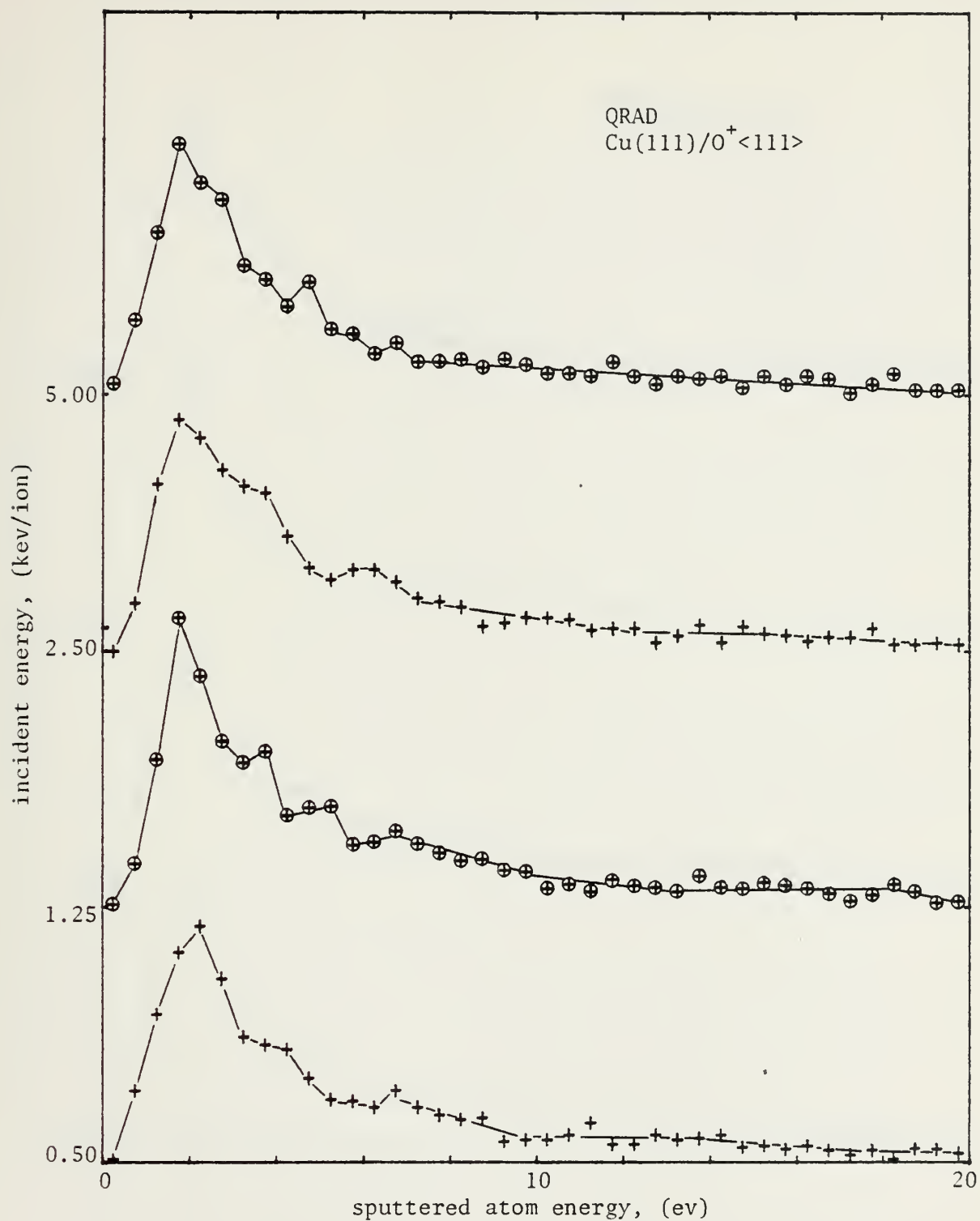


Fig. 17. QRAD normalized energy distributions of sputtered atoms, 0-20 ev.

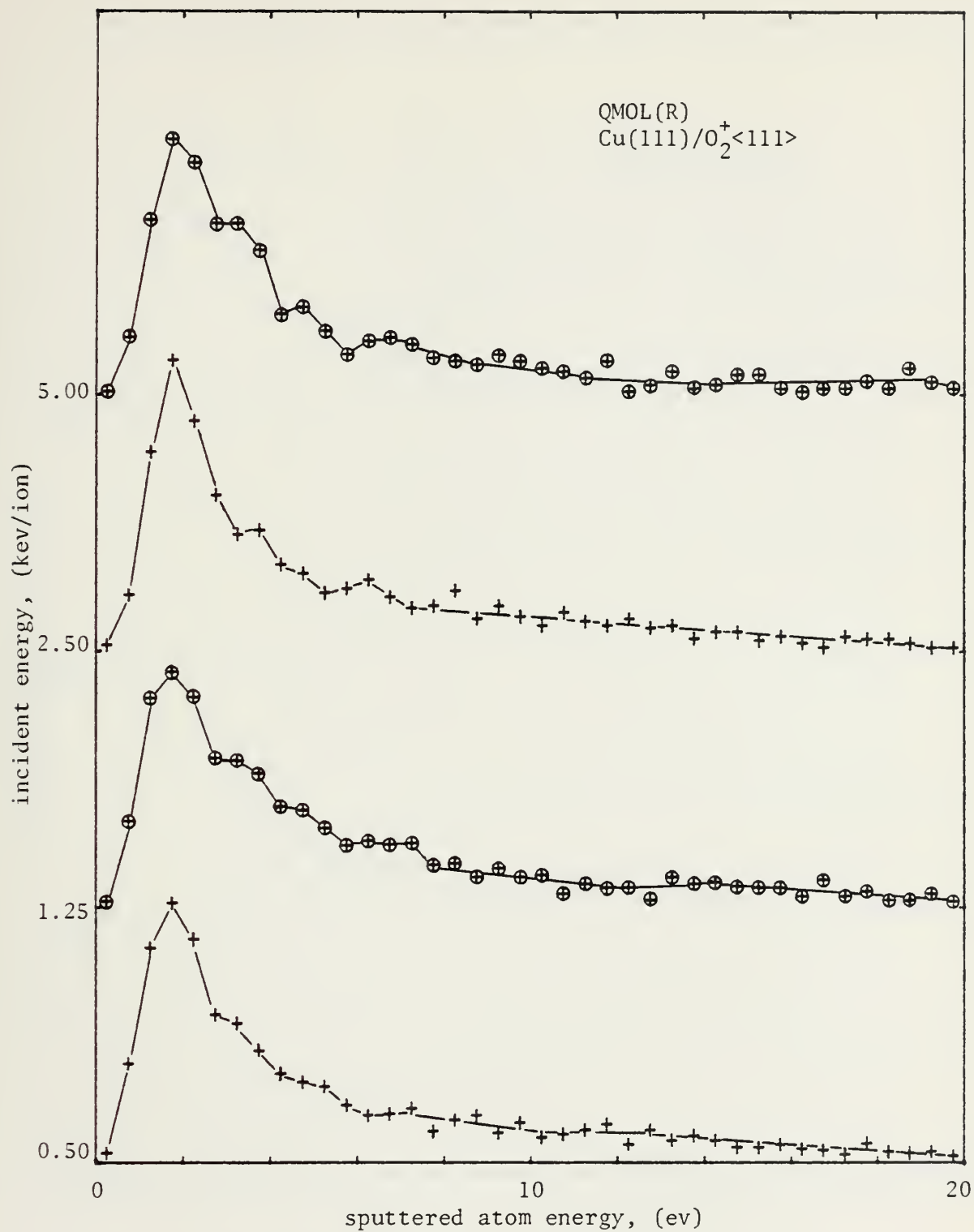


Fig. 18. QMOL(R) normalized energy distributions of sputtered atoms, 0-20 ev.

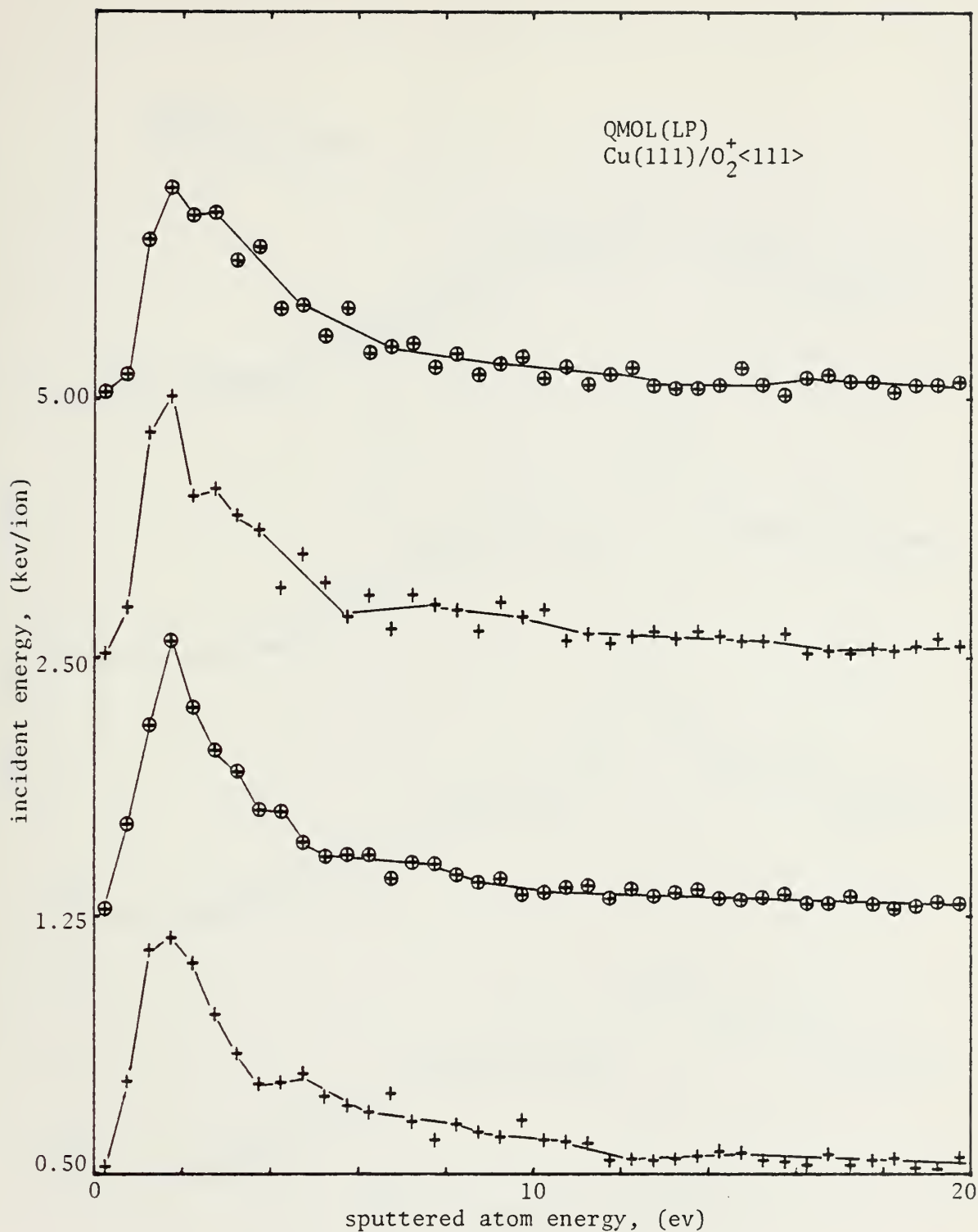


Fig. 19. QMOL(LP) normalized energy distributions of sputtered atoms, 0-20 ev.

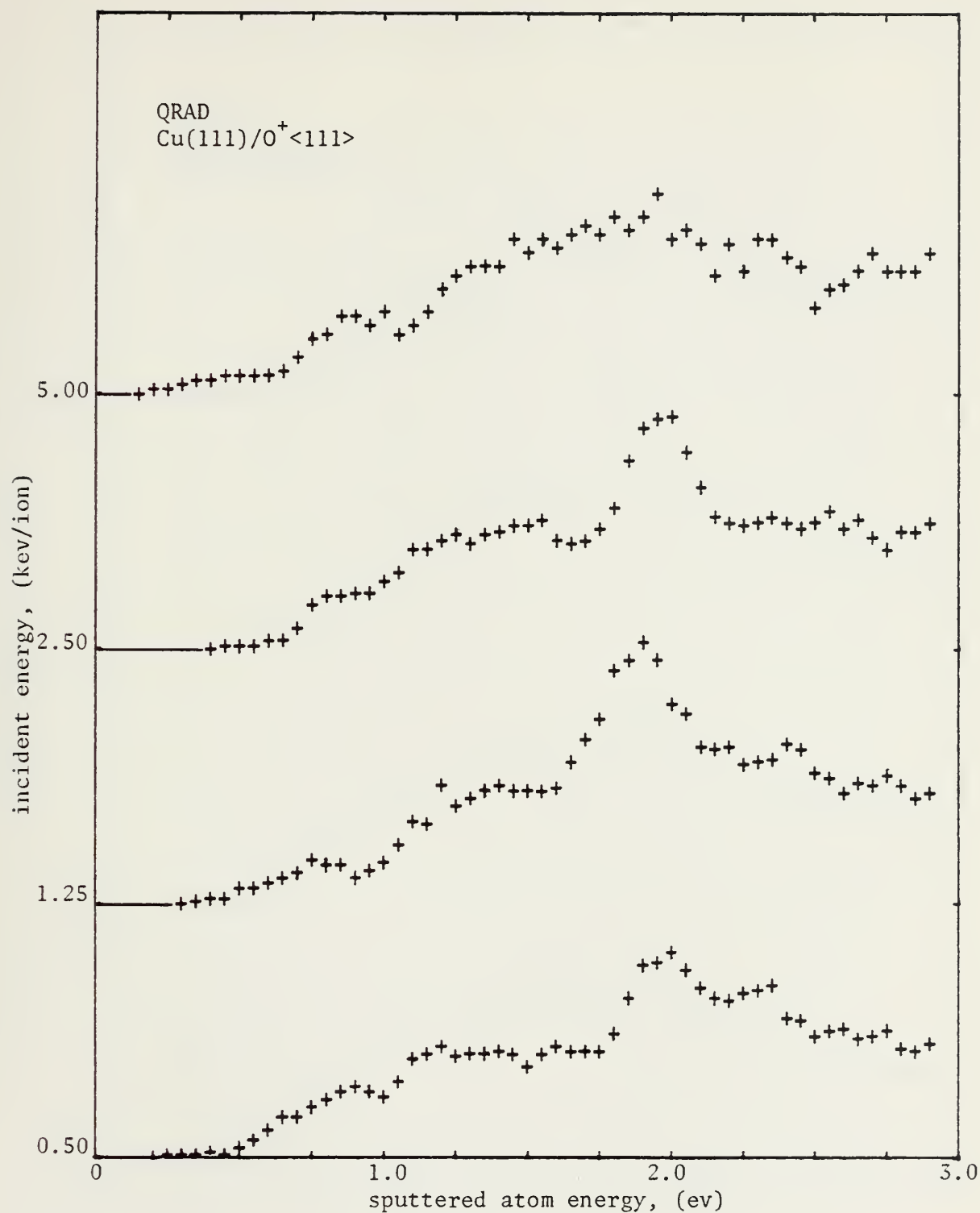


Fig. 20. QRAD normalized energy distributions of sputtered atoms, 0-3 ev.



Fig. 21. QMOL(R) normalized energy distributions of sputtered atoms, 0-3 ev.

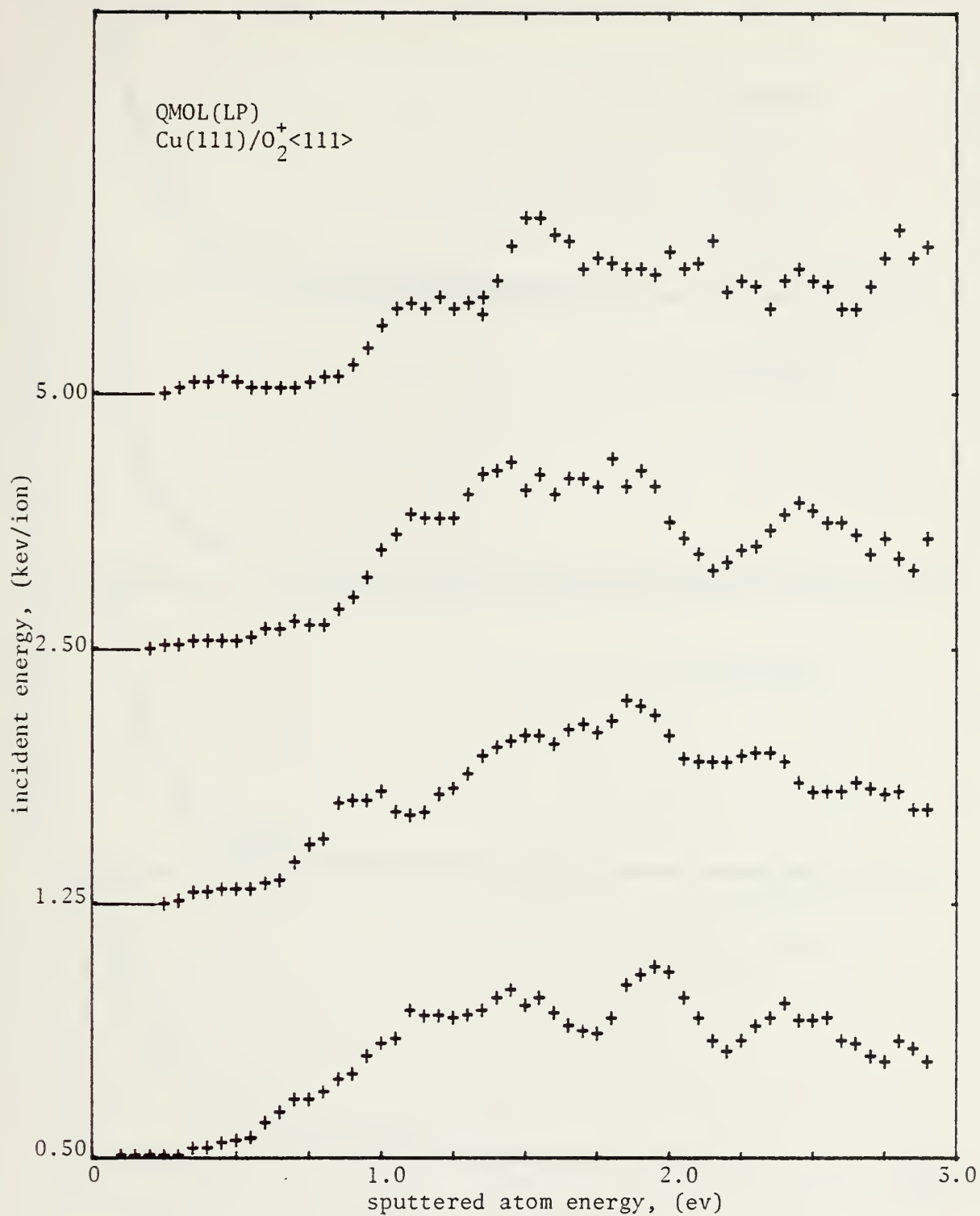


Fig. 22. QMOL(LP) normalized energy distributions of sputtered atoms, 0-3 ev.

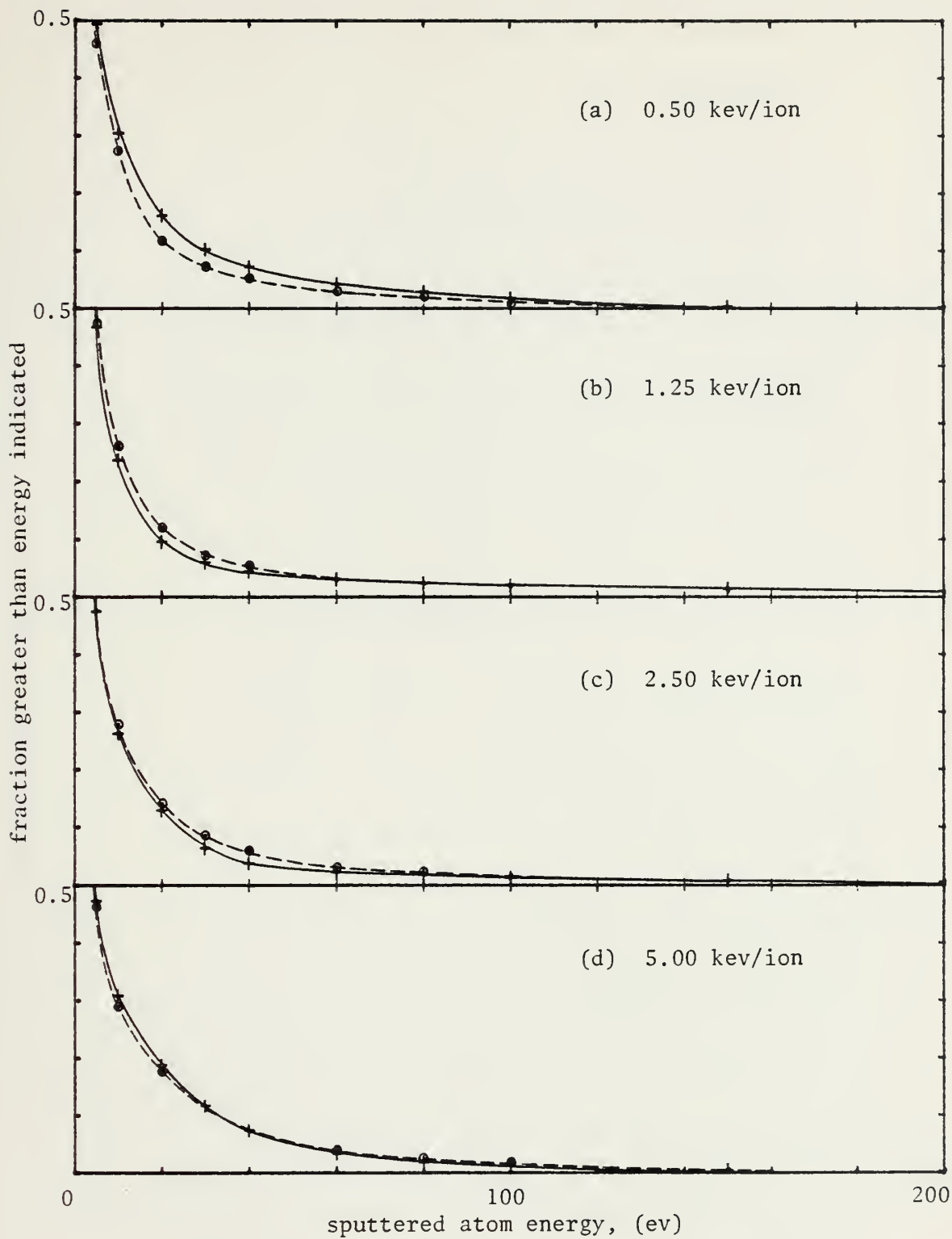


Fig. 23. Cumulative energy distributions of sputtered atoms.
(+ QRAD, o QMOL(R))

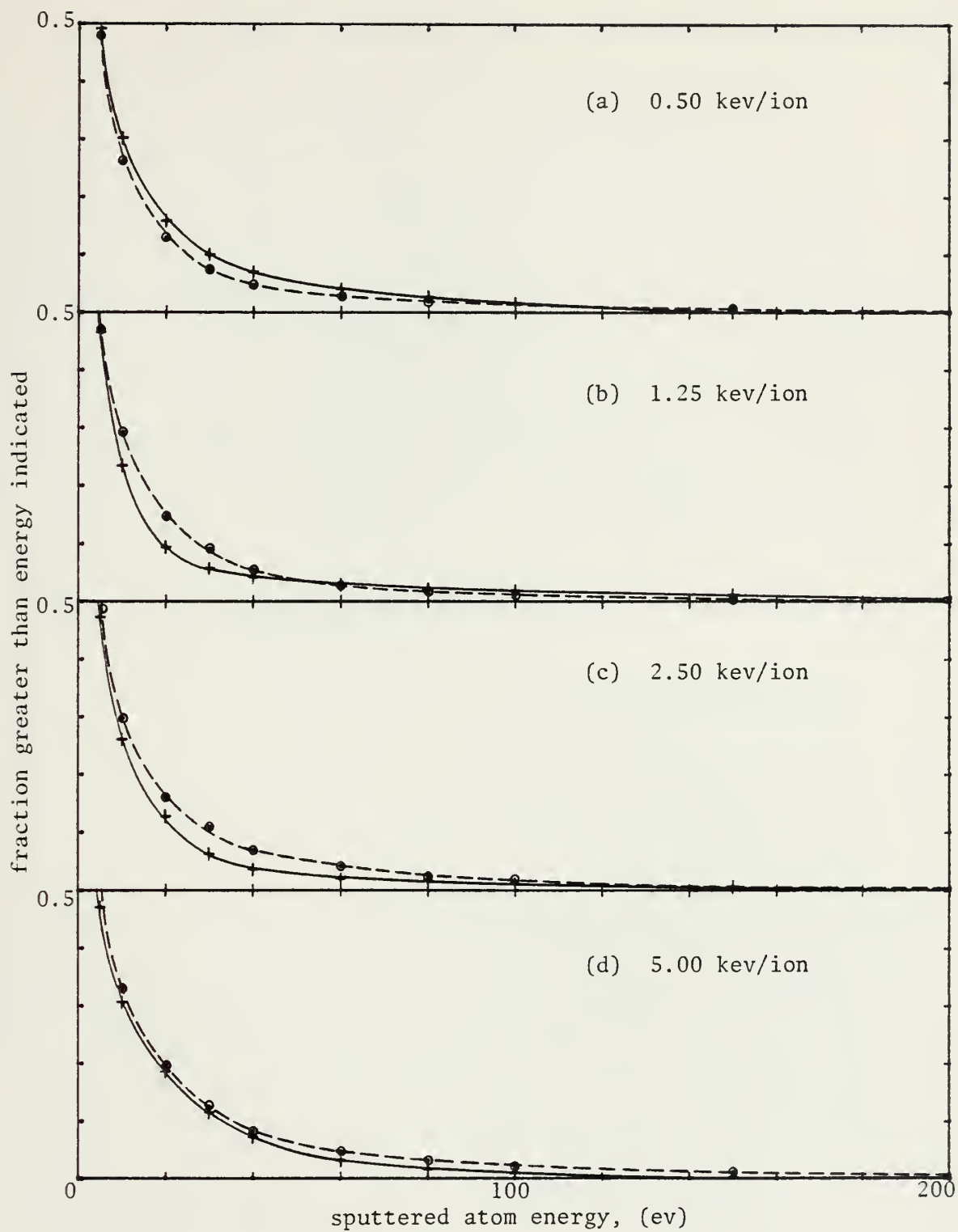


Fig. 24. Cumulative energy distributions of sputtered atoms.
 (+ QRAD, • QMOL(LP))

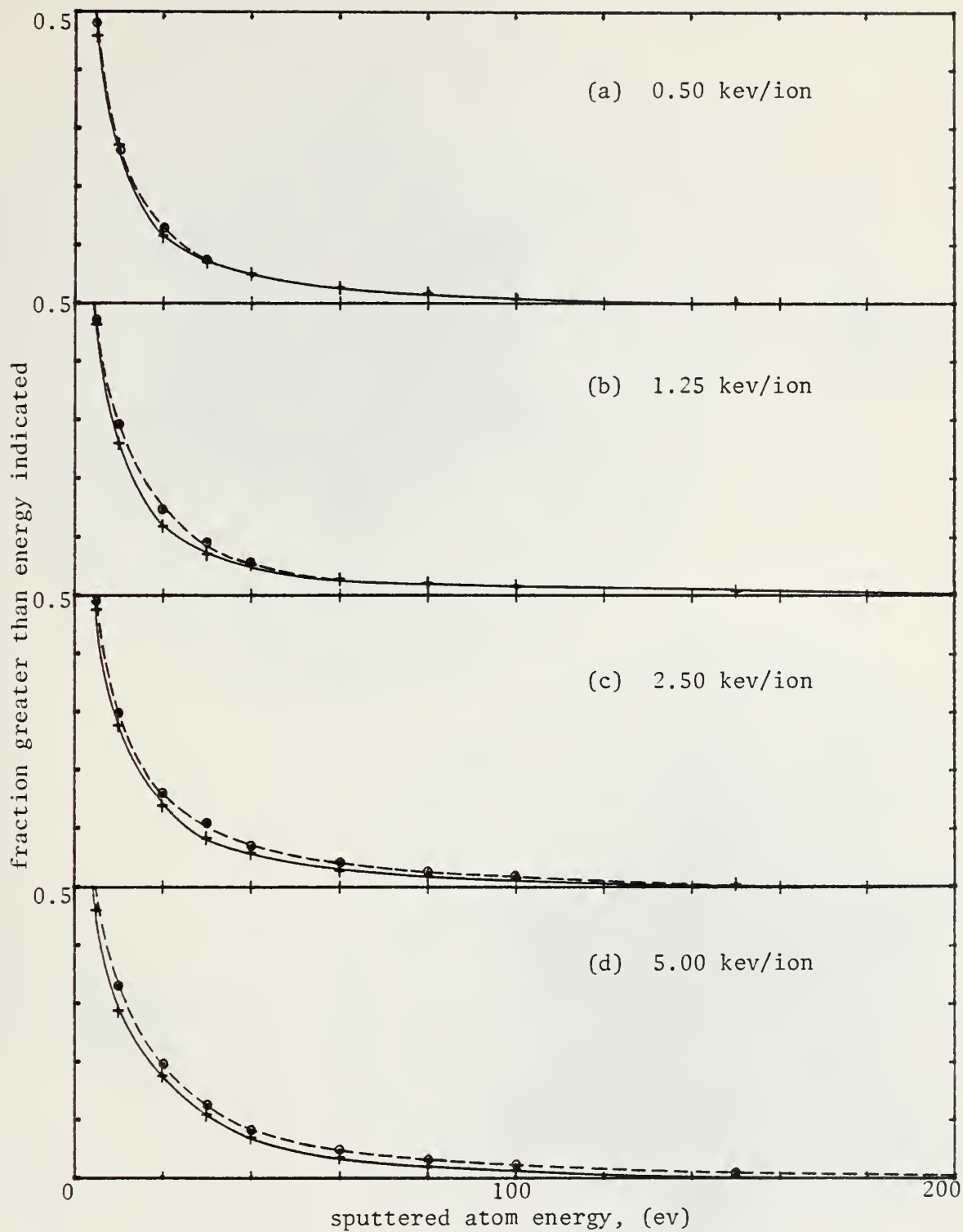
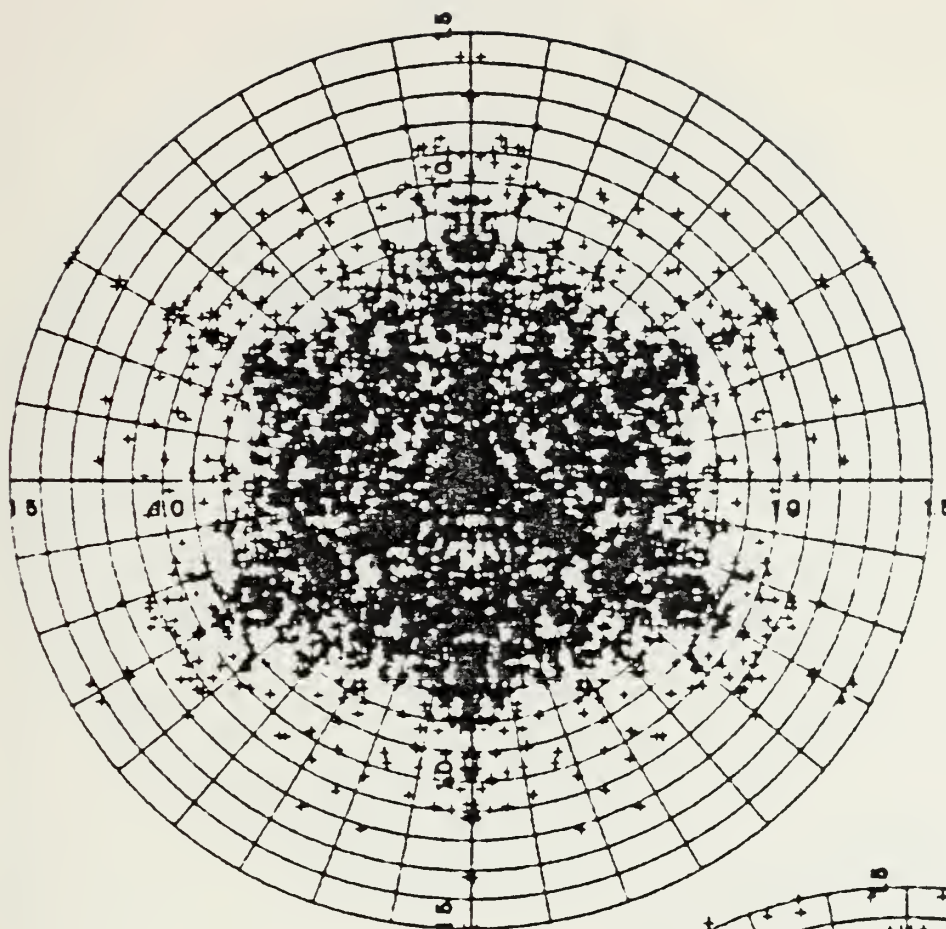
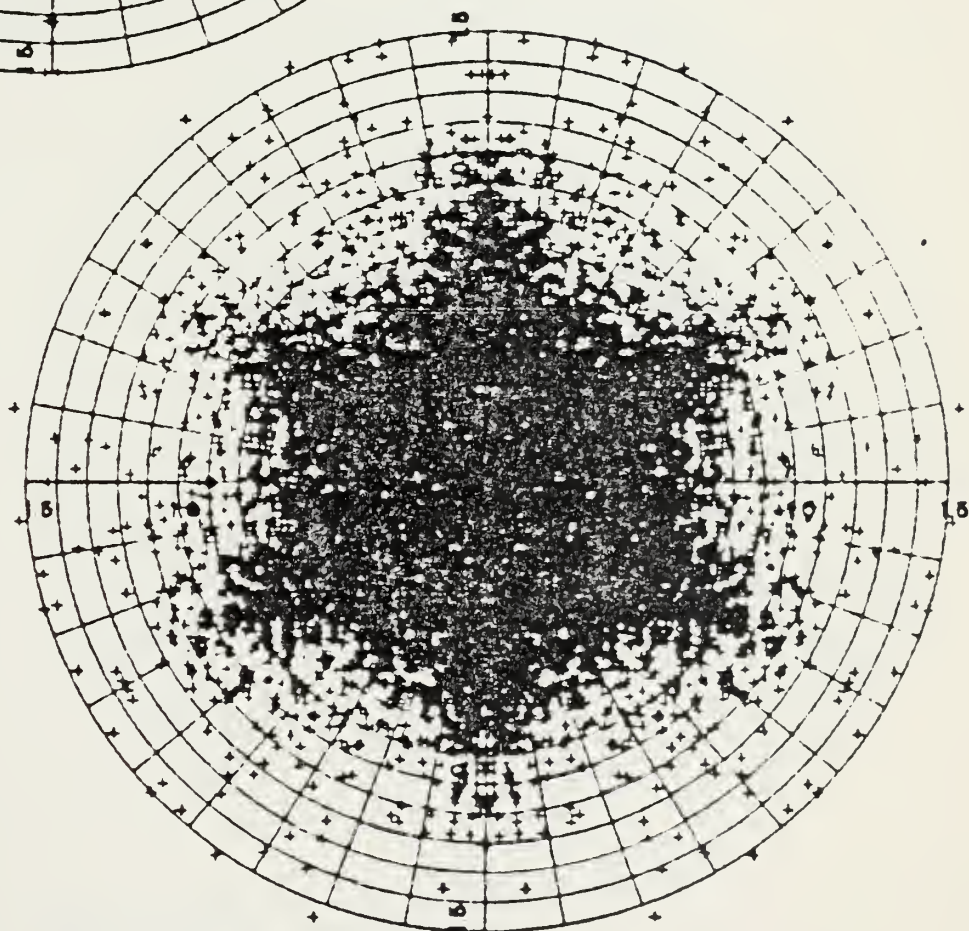


Fig. 25. Cumulative energy distributions of sputtered atoms.
 (+ QMOL(R), • QMOL(LP))

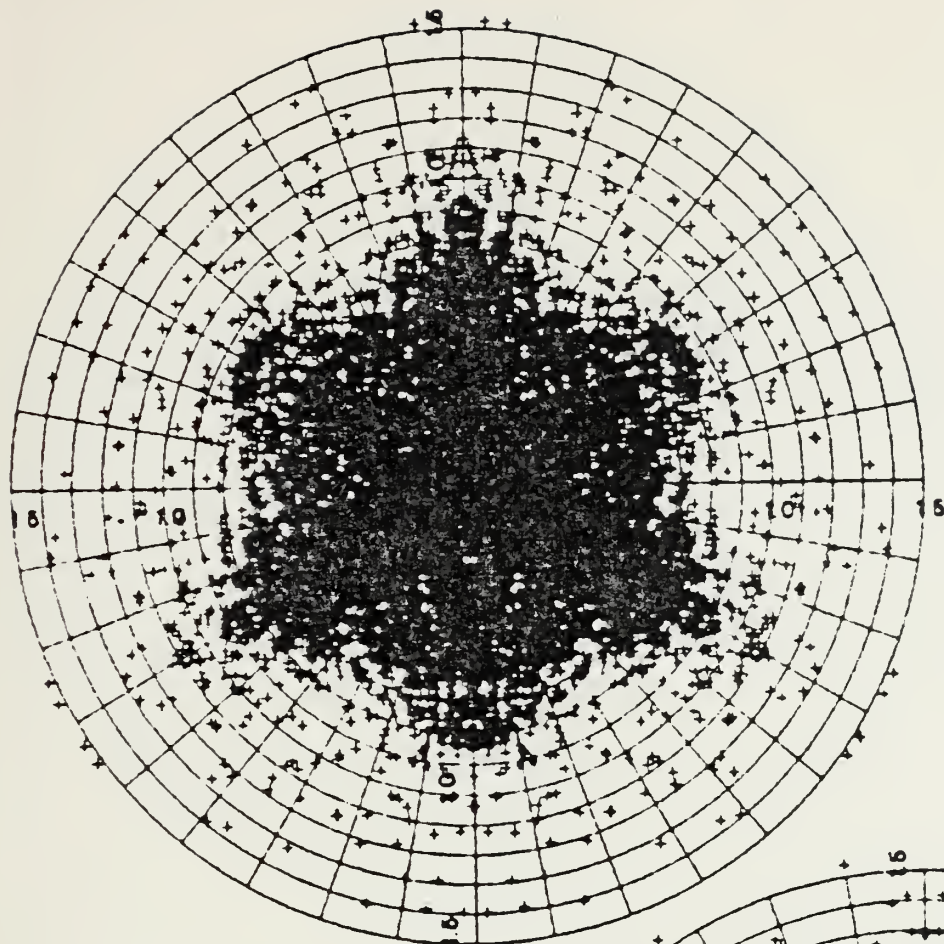


(a) QRAD
 $\text{Cu}(111)/\text{O}^+ \langle 111 \rangle$
 (15x4x12)

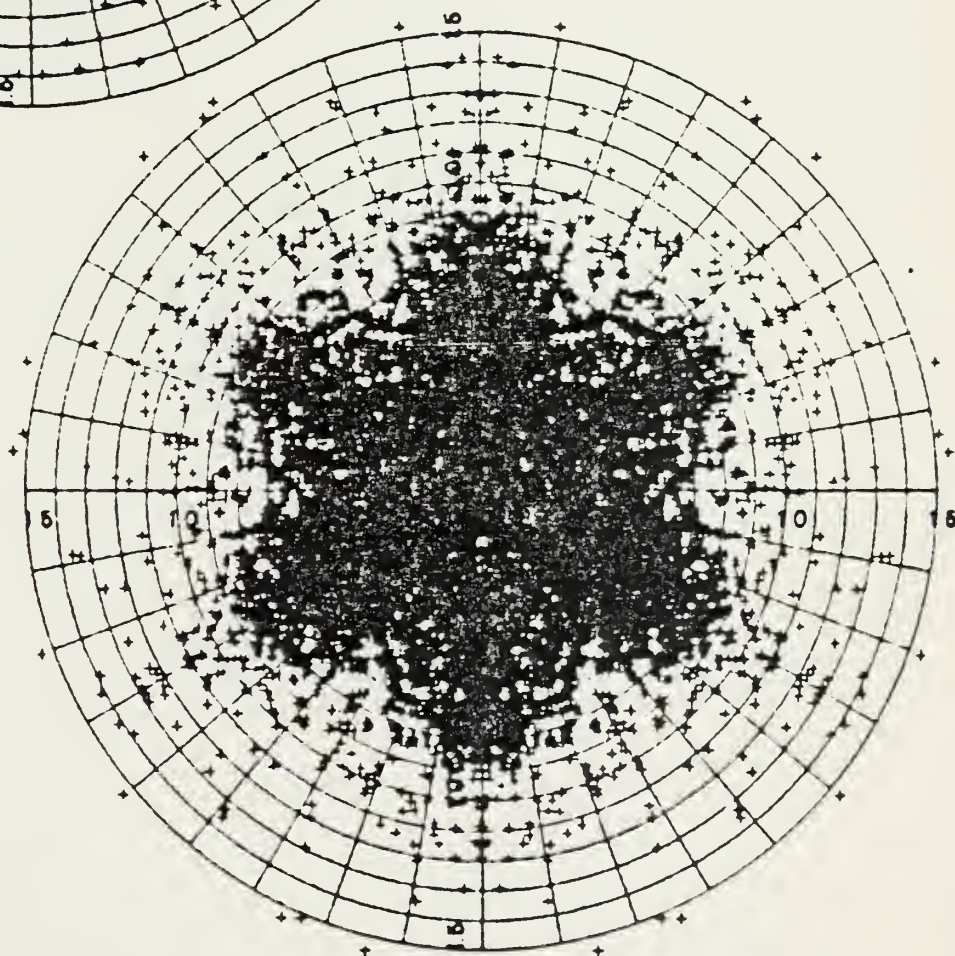


(b) QMOL(R)
 $\text{Cu}(111)/\text{O}_2^+ \langle 111 \rangle$
 (15x4x12)

Fig. 26. Spot patterns, 0.50 kev/ion.

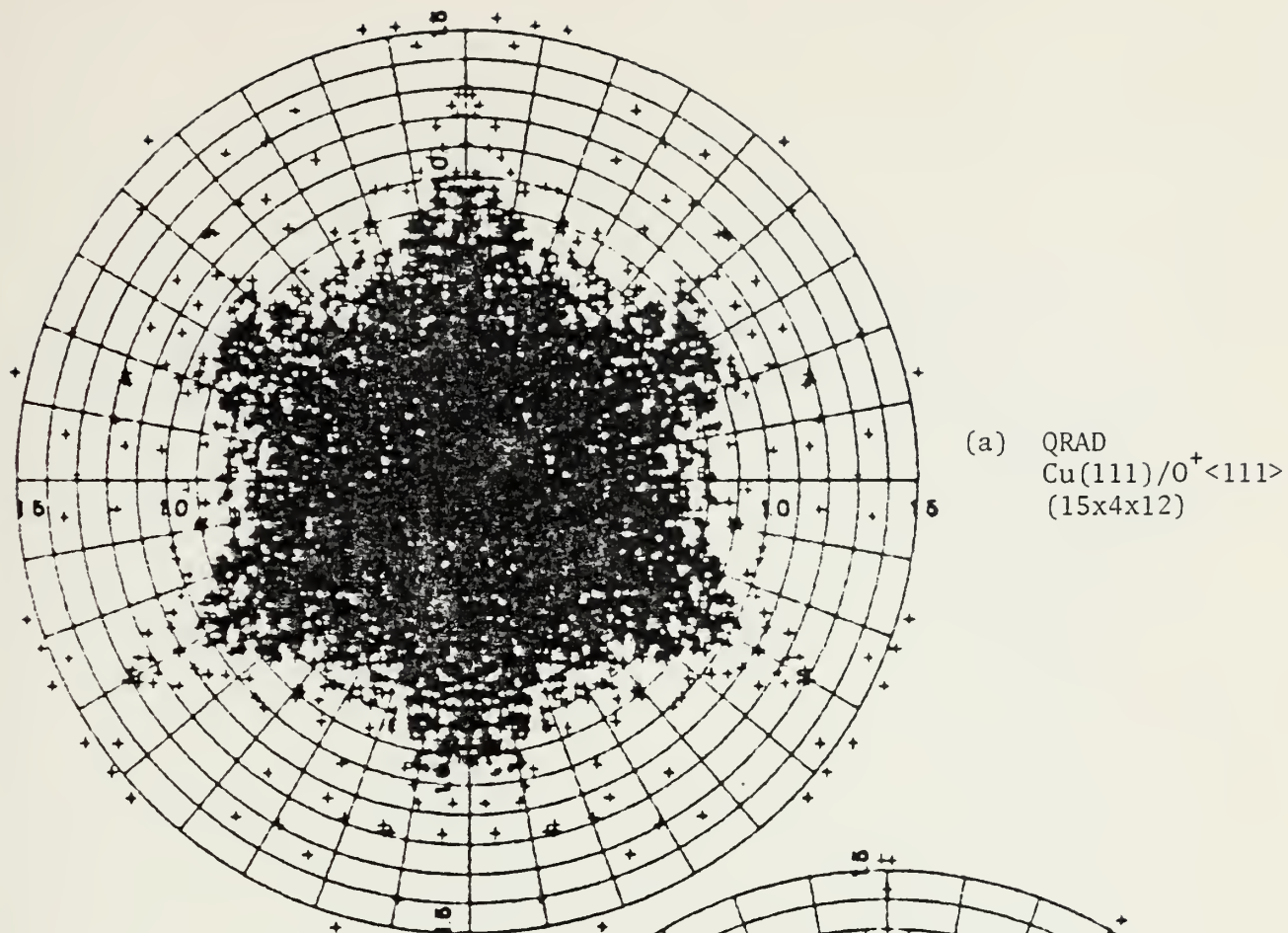


(a) QRAD
 $\text{Cu}(111)/\text{O}^+ \langle 111 \rangle$
 (15x4x12)



(b) QMOL(R)
 $\text{Cu}(111)/\text{O}_2^+ \langle 111 \rangle$
 (15x4x12)

Fig. 27. Spot patterns, 1.25 kev/ion.



(a) QRAD
Cu(111)/O⁺<111>
(15x4x12)

(b) QMOL(R)
Cu(111)/O₂⁺<111>
(15x4x12)

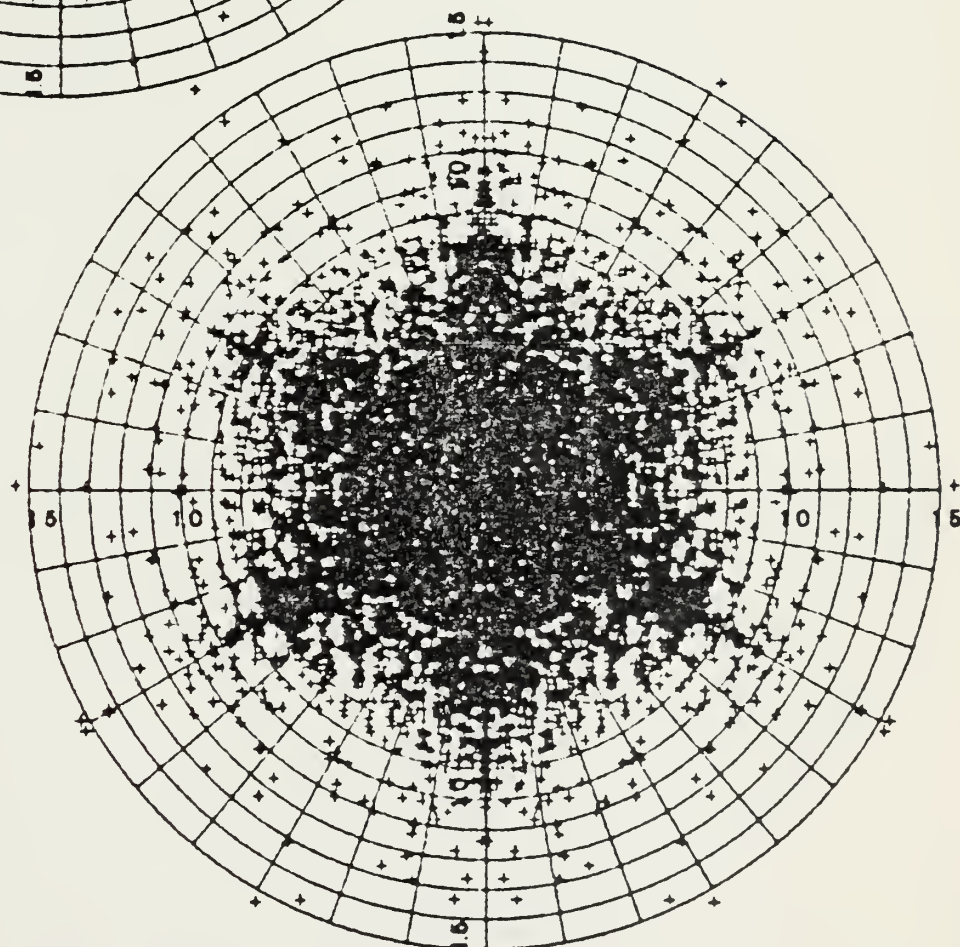
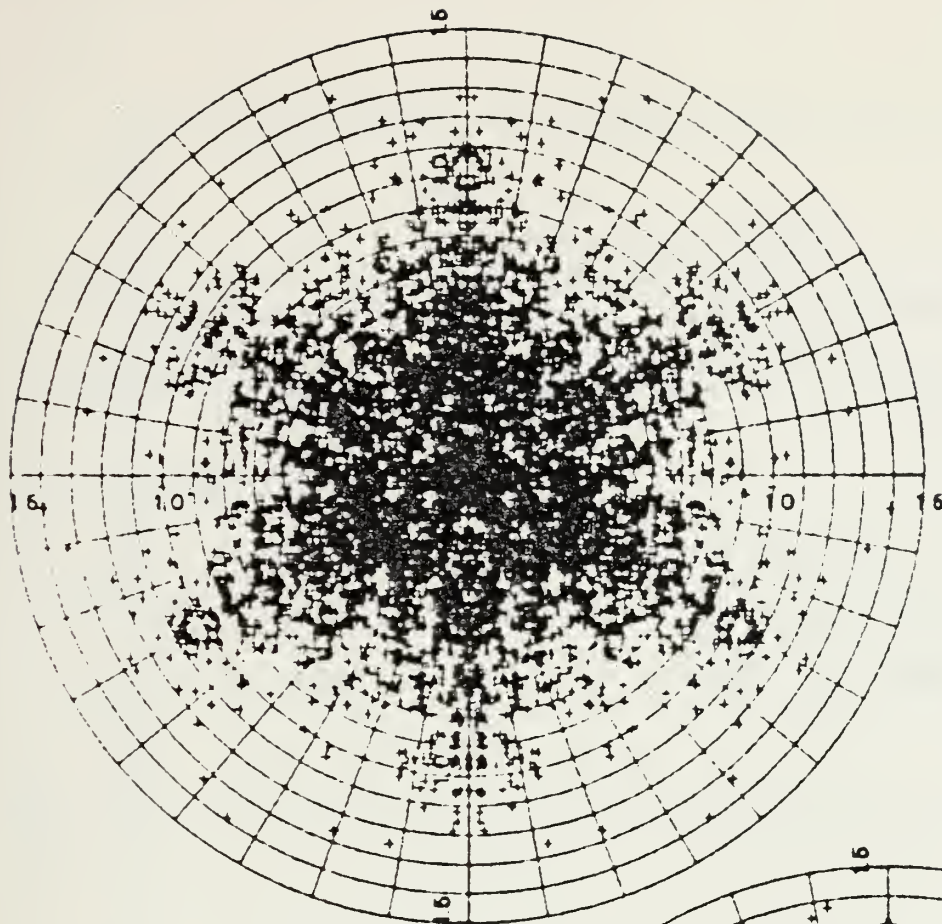
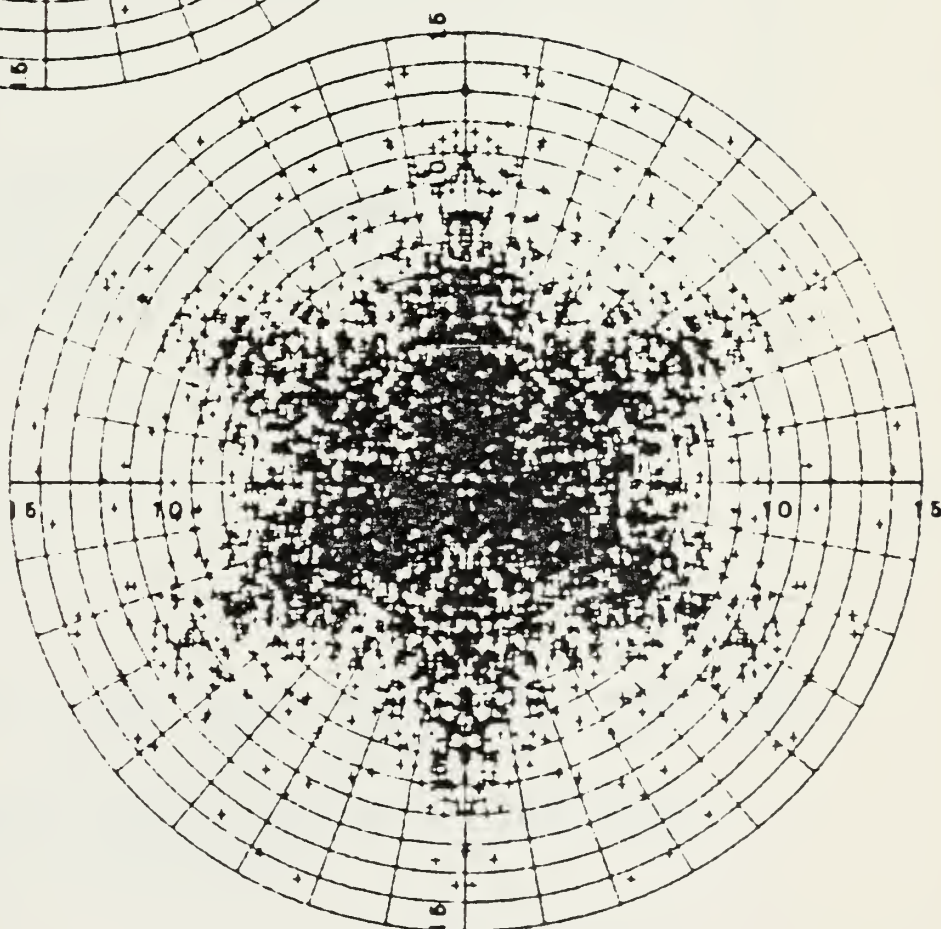


Fig. 28. Spot patterns, 2.50 kev/ion.



(a) QRAD
Cu(111)/O⁺<111>
(15x4x12)



(b) QMOL(R)
Cu(111)/O₂⁺<111>
(15x4x12)

Fig. 29. Spot patterns, 5.00 kev/ion.

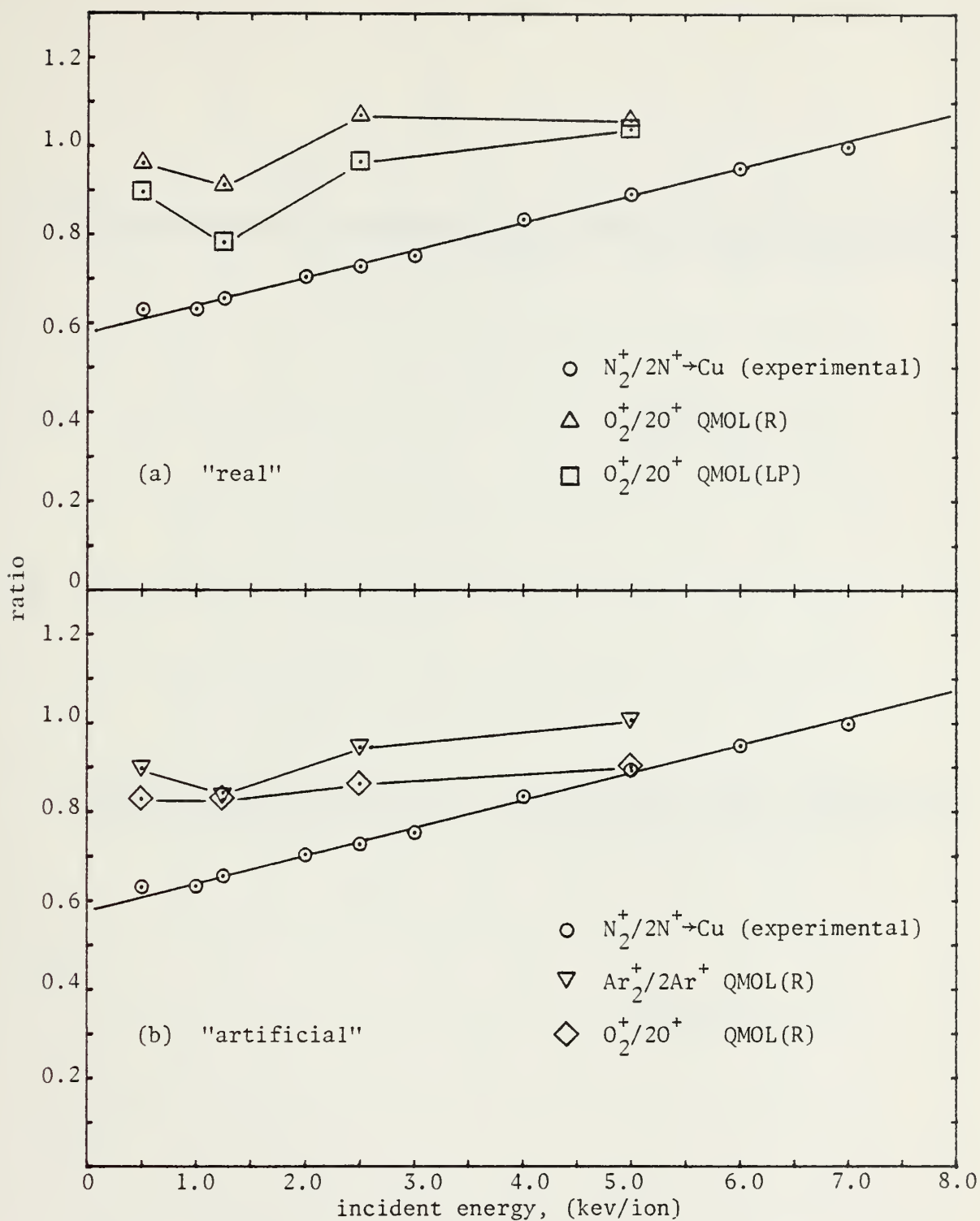


Fig. 30. Experimental [44] and simulation sputtering yield ratios vs. incident energy.

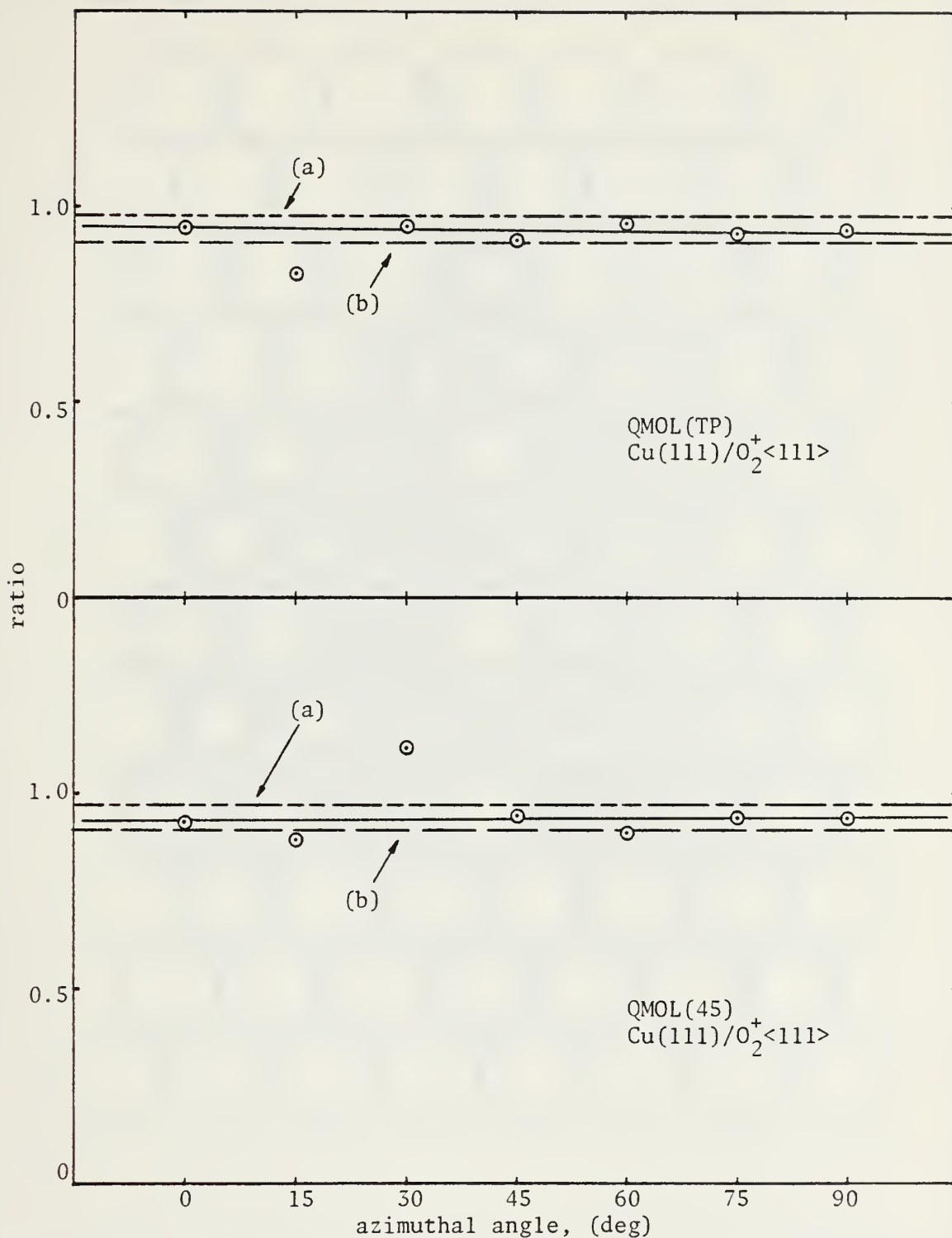


Fig. 31. Simulation sputtering yield ratio vs. azimuthal angle, ϕ_m , for QMOL(TP) and QMOL(45).
 (Line (a) is the QMOL(LP) avg. yield ratio; line (b) is the QMOL(LP) yield ratio at 1.25 kev/ion.)

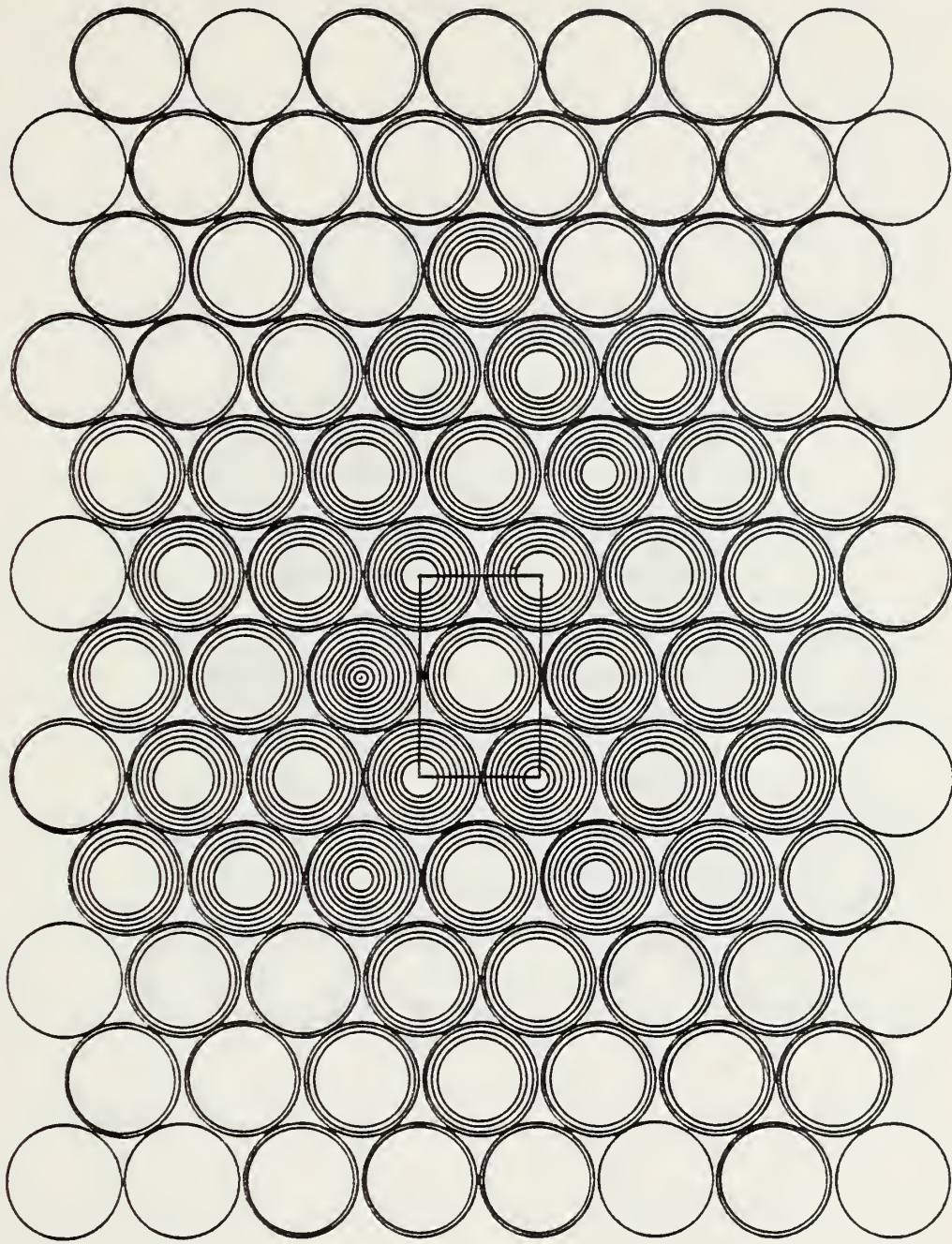


Fig. 32. QRAD normalized sputtering frequency, 0.50 kev/ion.
See text for explanation of scaling.

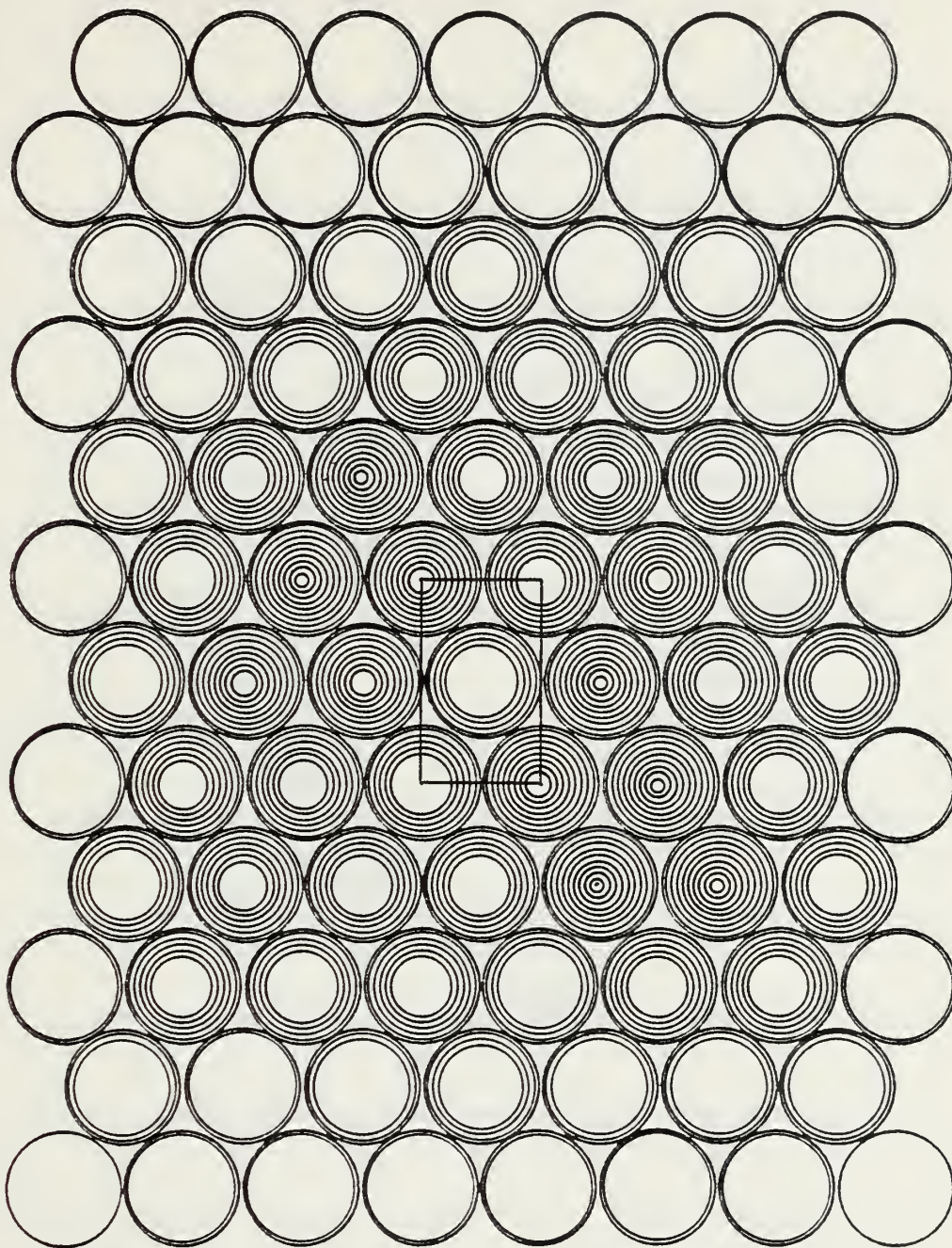


Fig. 33. QMOL(R) normalized sputtering frequency, 0.50 kev/ion.
See text for explanation of scaling.

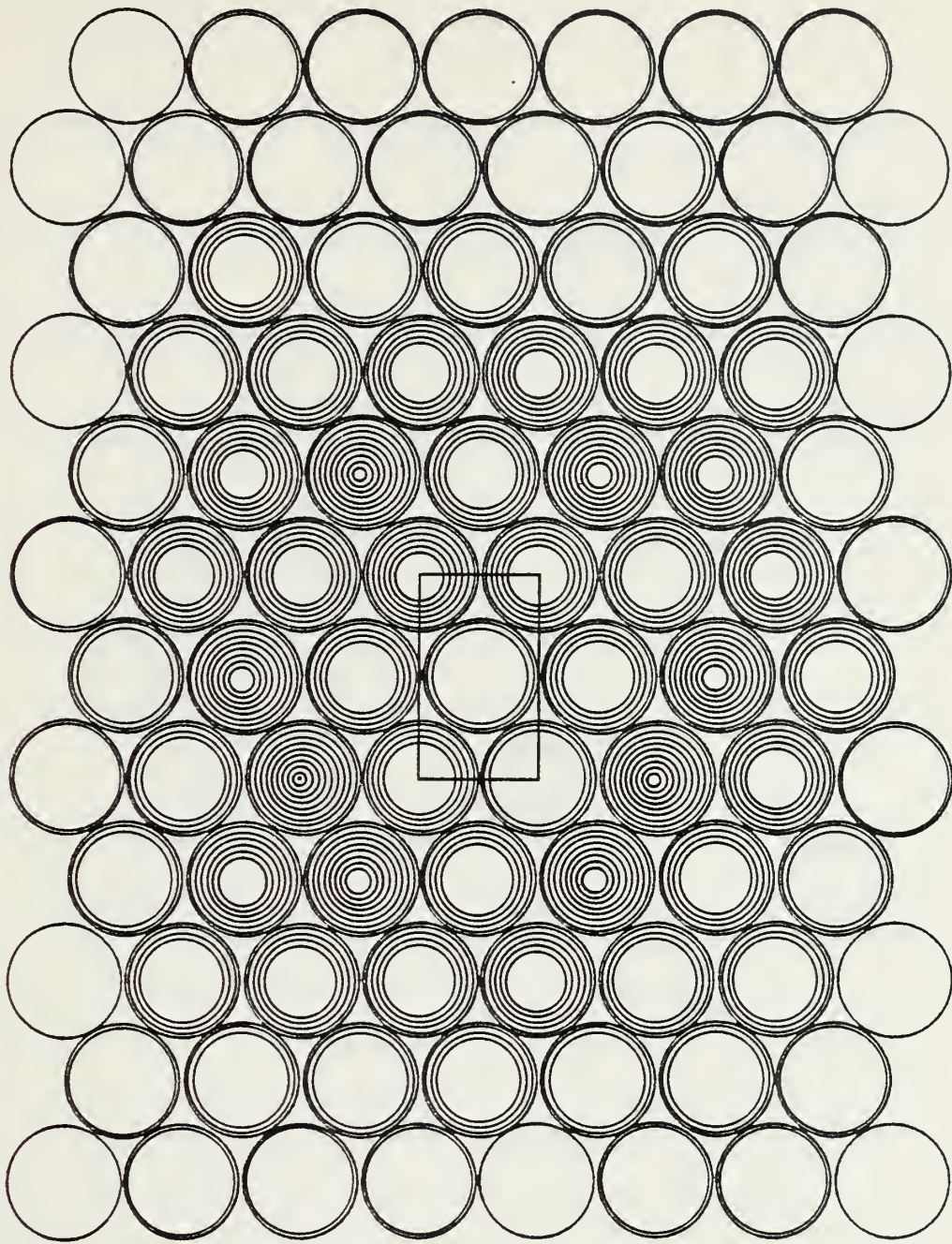


Fig. 34. QRAD normalized sputtering frequency, 1.25 kev/ion.
See text for explanation of scaling.

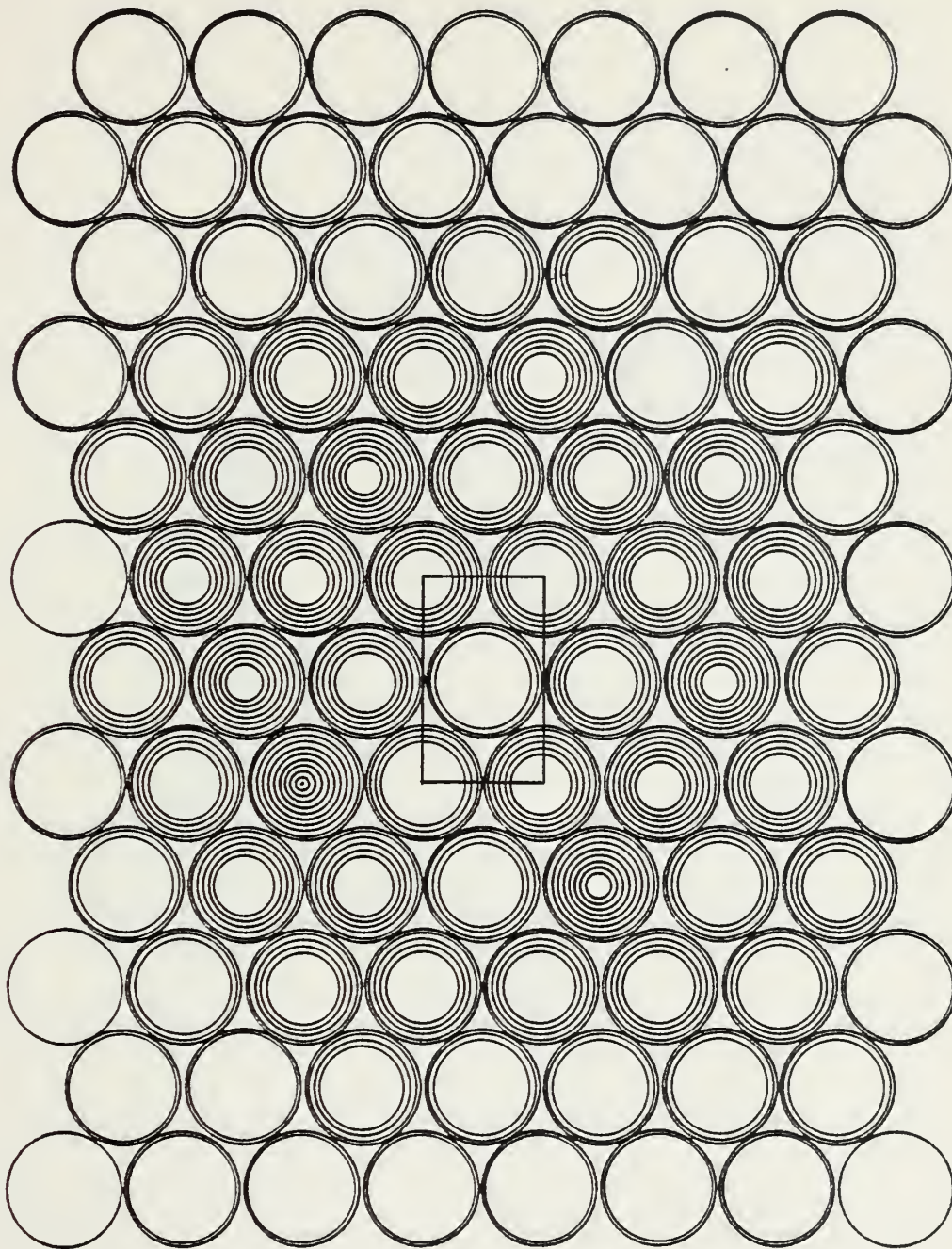


Fig. 35. QMOL(R) normalized sputtering frequency, 1.25 kev/ion.
See text for explanation of scaling.

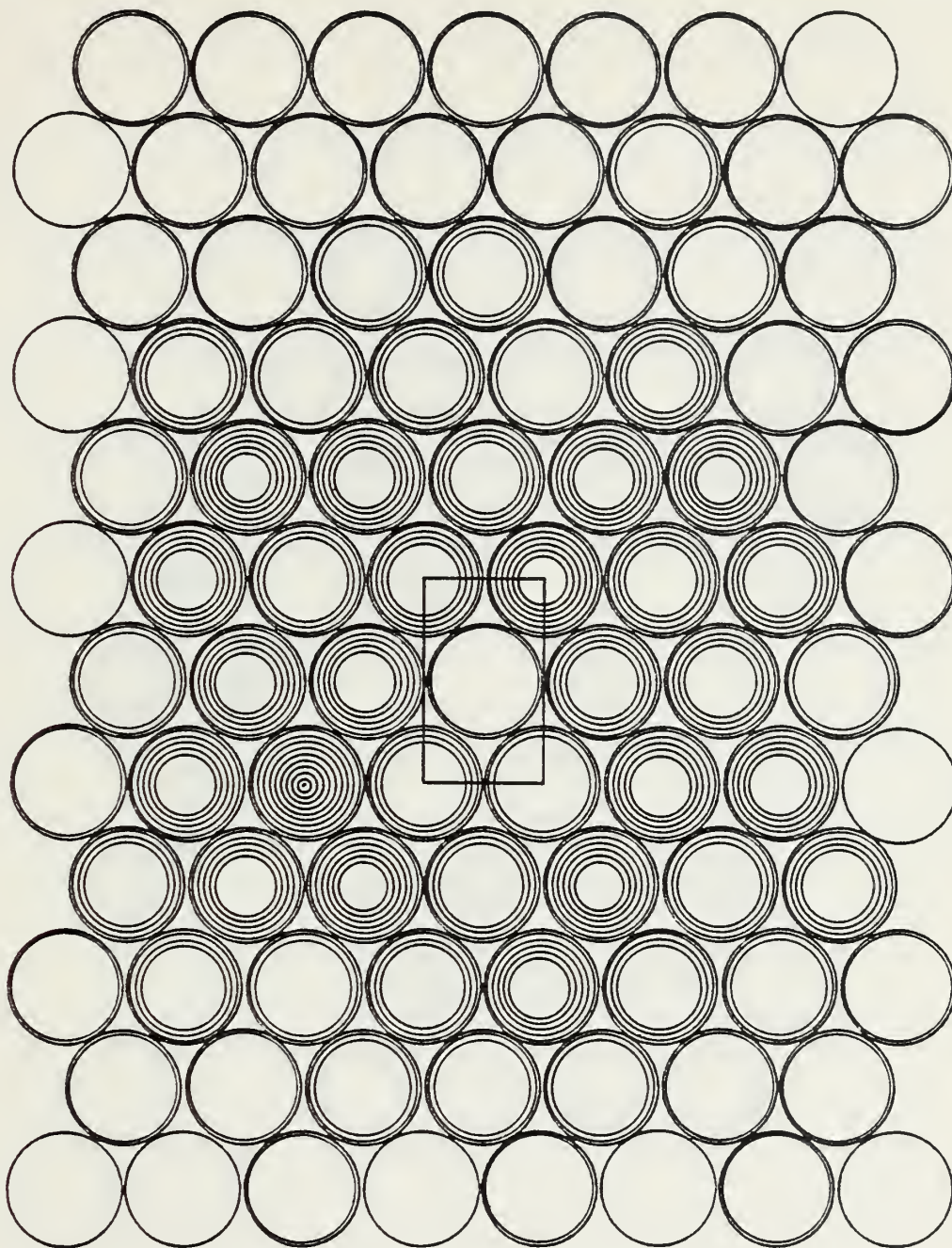


Fig. 36. QRAD normalized sputtering frequency, 2.50 kev/ion.
See text for explanation of scaling.

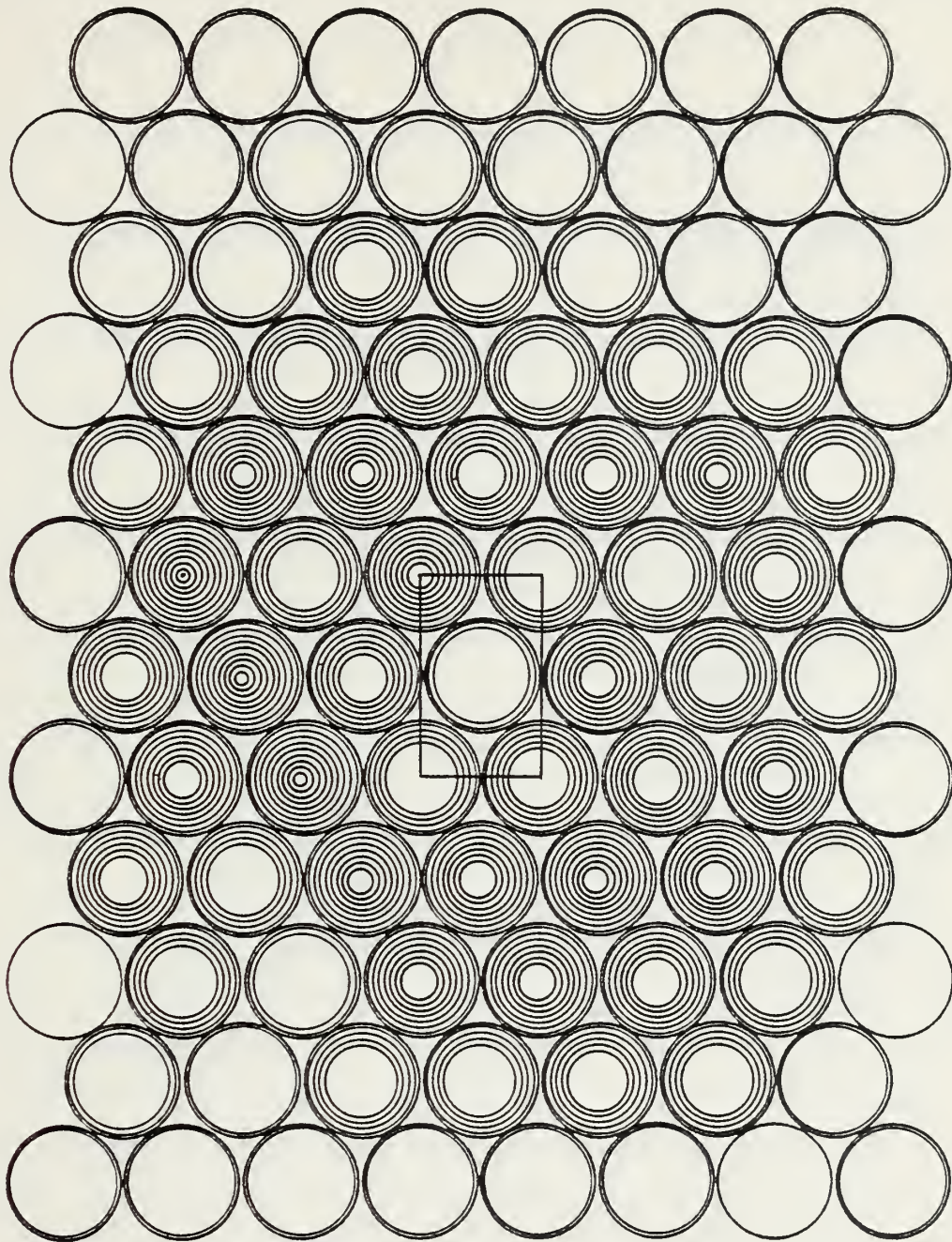


Fig. 37. QMOL(R) normalized sputtering frequency, 2.50 kev/ion.
See text for explanation of scaling.

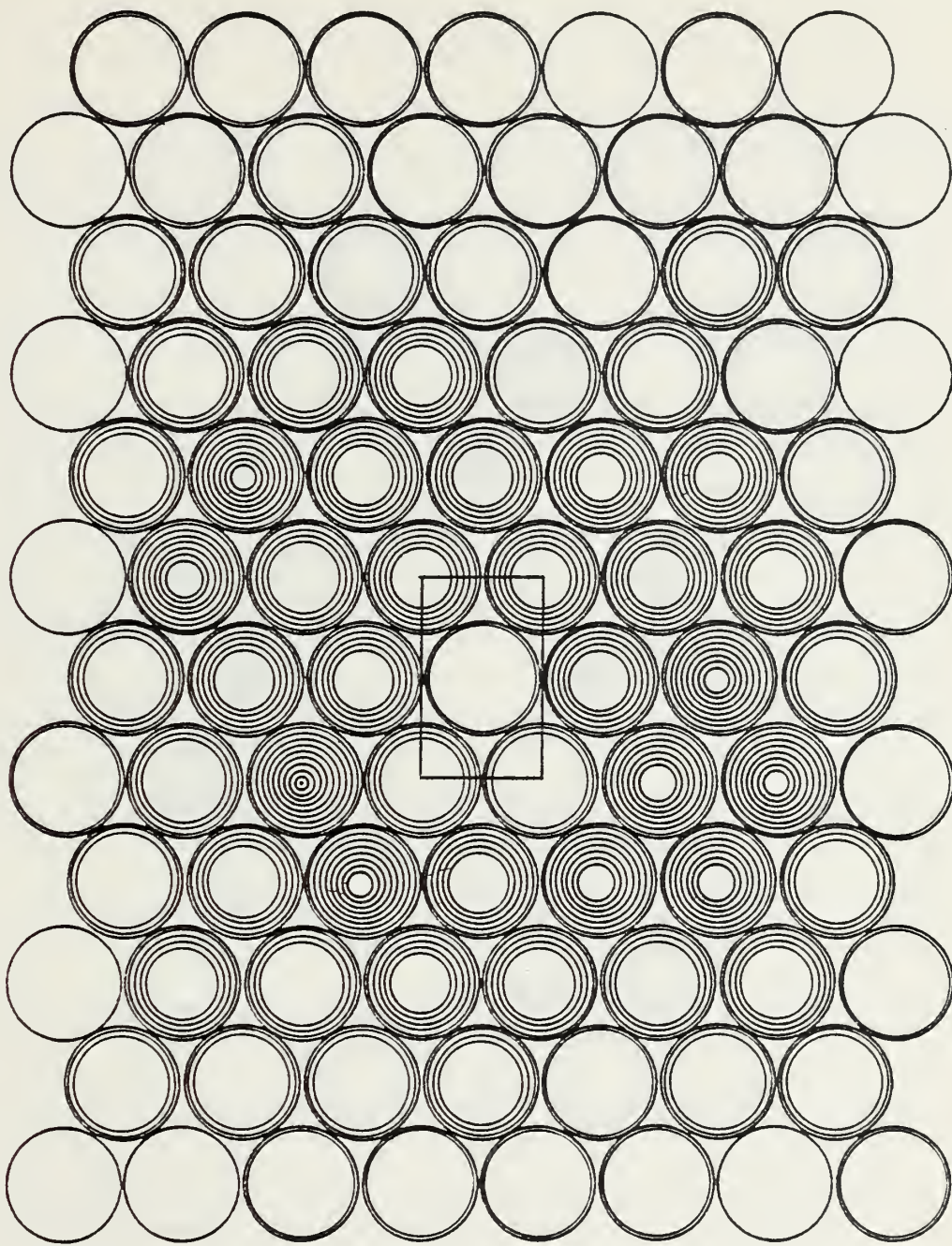


Fig. 38. QRAD normalized sputtering frequency, 5.00 kev/ion.
See text for explanation of scaling.

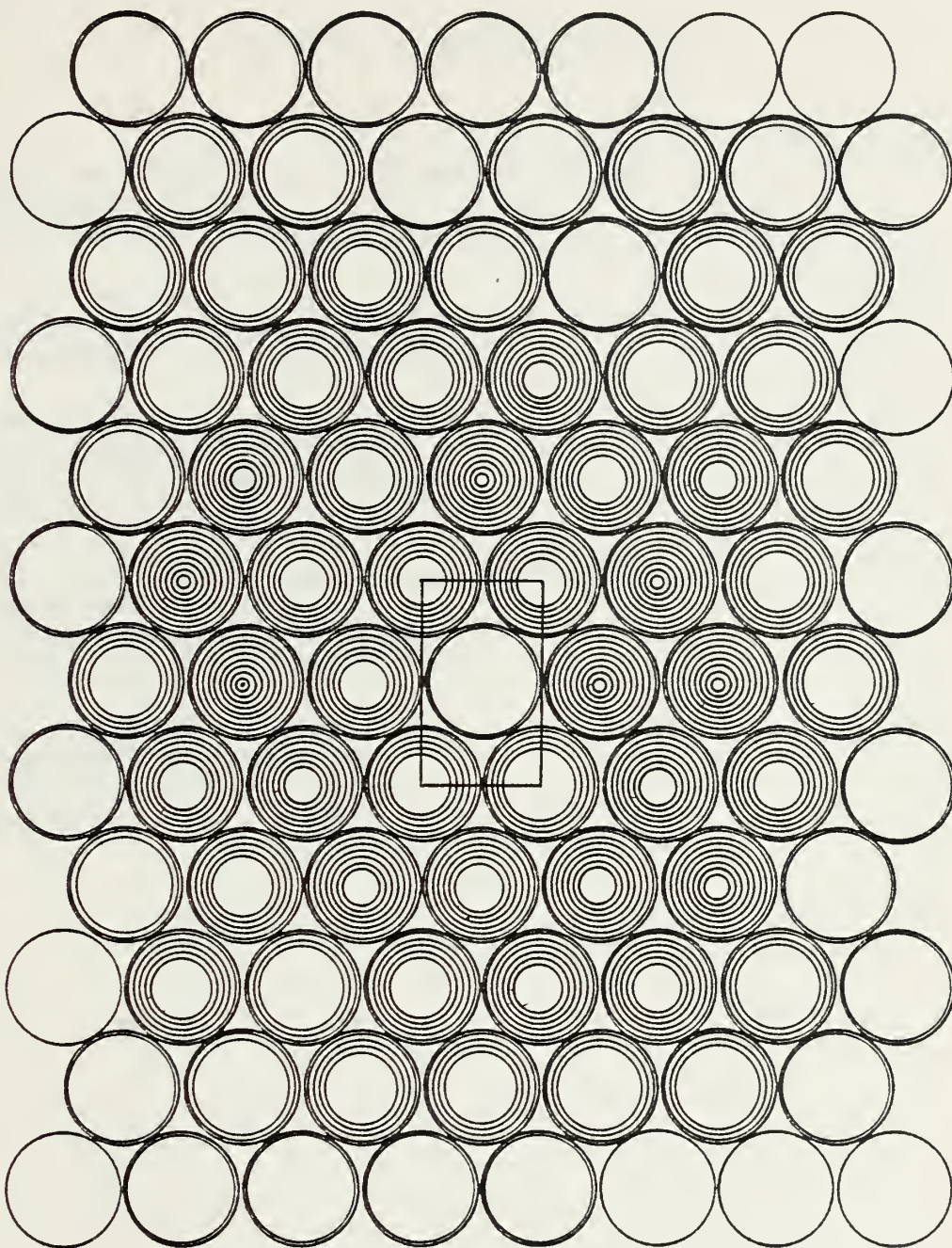


Fig. 39. QMOL(R) normalized sputtering frequency, 5.00 kev/ion.
See text for explanation of scaling.

INITIAL DISTRIBUTION LIST

	No. Copies
1. Defense Technical Information Center Cameron Station Alexandria, Virginia 22314	2
2. Library, Code 0142 Naval Postgraduate School Monterey, California 93940	2
3. Department Chairman, Code 61 Department of Physics Naval Postgraduate School Monterey, California 93940	2
4. Dr. Don E. Harrison, Jr., Code 61Hx Department of Physics Naval Postgraduate School Monterey, California 93940	5
5. Lt. William A. Mason, USN SWOSCOLCOM, Class 80 Department Head Course Newport, R.I. 02840	1

201618

Thesis

M3629 Mason
c.1

An investigation of
cascade energy density
effects using classical
trajectory simulations
of sputtering by
molecular ions.

201618

Thesis

M3629 Mason
c.1

An investigation of
cascade energy density
effects using classical
trajectory simulations
of sputtering by
molecular ions.

thesM3629

An investigation of cascade energy densi



3 2768 002 12496 8

DUDLEY KNOX LIBRARY